M 2016

NUMERICAL ANALYSIS OF THE TRANSPORT PHENOMENA ACROSS CLOTHING

MARTA SOFIA RAMOS DE OLIVEIRA SANTOS
DISSERTAÇÃO DE MESTRADO APRESENTADA
À FACULDADE DE ENGENHARIA DA UNIVERSIDADE DO PORTO EM
MESTRADO INTEGRADO EM ENGENHARIA QUÍMICA

Acknowledgements

Firstly, I would like to express my gratitude to Dr. Tiago Sotto Mayor, starting with the great opportunity he has given me by accepting me for this project. His guidance, encouragement, and utter commitment have truly turned this thesis into what it is. I would like to thank him for the countless stimulating discussions, patience, and for teaching me far more than science. I would also like to acknowledge Prof. João Campos, for his kind help and suggestions.

Thanks are also due to EMPA St. Gallen, for its financial support, and for warmly receiving students such as myself, creating a friendly working environment, to which I was happy to return to everyday.

I am grateful to my family, and to my boyfriend, for being so supportive of my decision and for carrying me through all the ups and downs. To my newly found friends in Switzerland, be they housemates, travel partners, or fellow researchers in EMPA, thank you for making sure there were far more ups than downs.

Abstract

Flow and heat transfer in clothing microclimates close to the skin have been numerically investigated. Simulations were performed considering a horizontal impermeable cylinder (human limb) surrounded by a porous layer (fabric) and exposed to cool external air. The main purpose of this study is to analyse the local and average effects of varying the air gap thickness, the permeability of the fabric, and the emissivity of the inner surface of the fabric. Such a study is relevant, for instance, for protective clothing applications (e.g. CBRN clothing), for which the local variations in temperature and/or heat fluxes may cause discomfort and health-related problems for the user, rendering space-averaged approaches inadequate. A second goal of this project is to assess the relative importance of natural convection.

Transient-state simulations were conducted for a 2D cross-section of the clothed limb using COMSOL Multiphysics, in which Reynolds number was kept constant at 3900 (turbulent flow). Results reveal that increasing the air gap thickness causes substantial changes in the temperature and heat flux fields, due to the increased importance of natural convection. Decreasing fabric permeability or emissivity is shown to overall decrease the local heat fluxes. It was further concluded that the role of natural convection is non-negligible, and in some cases central, to local flow and heat transfer.

The present study demonstrates that the magnitude (and relative importance) of the various heat transfer mechanisms can be altered, by varying the mentioned parameters. This means that heat transfer is significantly influenced by the fit and physical properties of the clothing, which can be engineered to reduce its adverse effects.

Keywords: cylindrical microclimates, air gap, permeability, emissivity, air flow, turbulence, heat transfer, natural convection, radiation, computational fluid dynamics, protective clothing

Sumário

O escoamento e transporte de calor em microclimas próximos da pele foram investigados numericamente. Foram realizadas simulações considerando um cilindro horizontal impermeável (um membro do corpo humano) rodeado de uma camada porosa (tecido), e exposto a correntes de ar fresco exterior. O principal objetivo deste estudo é a análise dos efeitos locais e médios da variação da espessura da camada de ar, da permeabilidade do tecido, e da emissividade da superfície interna do tecido. Tal estudo é relevante, por exemplo, para aplicações relacionadas com vestuário protetor (ex: vestuário CBRN), para as quais as variações locais de temperatura e/ou fluxos de calor poderão provocar desconforto ou problemas de saúde no utilizador, tornando desadequadas as abordagens médias no espaço. Um segundo objetivo deste projeto prende-se com a avaliação da importância relativa da convecção natural.

Foram levadas a cabo simulações em estado transiente para um corte transversal (2D) do membro vestido com recurso ao COMSOL Multiphysics, nas quais o número de Reynolds foi mantido constante e igual a 3900 (escoamento turbulento). Os resultados revelam que o aumento da espessura da camada de ar provoca alterações substanciais nos campos de temperatura e de fluxo de calor, devido ao aumento da importância da convecção natural. A diminuição da permeabilidade ou emissividade do tecido leva, de um modo geral, à diminuição dos fluxos de calor locais. Concluiu-se ainda que o papel da convecção natural é não negligenciável, e por vezes central, no escoamento e transferência de calor a nível local.

O presente estudo demonstra que a magnitude (e importância relativa) dos vários mecanismos de transferência de calor pode ser alterada, através da variação dos parâmetros mencionados. Isto significa que a transferência de calor é significativamente influenciada pelo ajuste da roupa ao corpo, bem como pelas propriedades físicas do tecido, os quais podem ser escolhidos de forma a reduzir os seus efeitos adversos.

Palavras-chave: microclimas cilíndricos, camada de ar, permeabilidade, emissividade, escoamento de ar, turbulência, transferência de calor, convecção natural, radiação, computational fluid dynamics, vestuário protetor

Declaração

Declara, sob compromisso de honra, que este trabalho é original e que todas as contribuições não originais foram devidamente referenciadas com identificação da fonte.

Table of Contents

Figures and Tables

Nomenclature

A	Area	m^2
C_p	Specific heat capacity	$\mathrm{J/(\,kg\,K)}$
D	Characteristic diameter	m
D_0	Diameter of the limb	m
D_1	Diameter of the outer fabric	m
D_2	Diameter of the computational domain	m
Da	Darcy number	-
E	Total energy	J/kg
f	Vortex shedding frequency	1/s
$\vec{F}$	Force vector	N
$g, \vec{g}$	Gravitational acceleration and vector	m/s
Gr	Grashof number	-
H	Thickness	m
I	Turbulence intensity	-
I_c	Ratio between fabric's thickness and outer diameter of the fabric (H_fab/D_1)	-
I_g	Ratio between air gap's thickness and outer diameter of the fabric (H_gap/D_1)	-
k	Thermal conductivity	W/(m K)
K	Permeability (reciprocal of viscous resistance)	m^2
L_T	Turbulence length scale	m
L_rec	Recirculation length	m
l_w	Distance to the closest wall	m
Ma	Mach number	-
$\vec{N}$	Surface normal vector	-
Nu	Nusselt number (hD/k)	-
p	Pressure	Pa
q	Heat flux	$\mathrm{W/m}^2$
Ra	Rayleigh number	-
R_CT	Thermal resistance of the fabric layer	$\mathrm{m}^2\mathrm{K/W}$
Re	Reynold's number ($\rho UD/\mu$)	-
R_t	Turbulent Reynold's number	-
St	Strouhal number (fD/U)	-

t	Time	s
t_0	First time at which flow can be considered periodic	s
T	Temperature	K
TKE	Turbulent kinetic energy	$\mathrm{m^2/s^2}$
u, v	Fluid velocity components in the x- and y- direction	$\mathrm{m/s}$
U	Fluid velocity magnitude	$\mathrm{m/s}$
x, y	Space coordinates	m

Greek letters:

α	Thermal diffusivity ($k/(\rho C_p)$)	$\mathrm{m^2/s}$
β	Thermal expansion coefficient	$\mathrm{1/K}$
γ	Porosity, ratio between volume of fluid and volume of solid	-
ε	Emissivity	-
μ	Dynamic viscosity	Pa s
ν	Kinematic viscosity	$\mathrm{m^2/s}$
ρ	Density	$\mathrm{kg/m^3}$
θ	Angular coordinate, $\theta = 0°$ corresponding to the upstream side of the clothed limb and $\theta = 90°$ to the point at the surface of the clothing with maximum y-coordinate	°

Subscripts:

∞	Far field (free stream)
air	Air
avg	Average
f	Fluid
fab	Fabric
gap	Air gap
in	Inlet
K	Permeability-based
max	Maximum
out	Outlet
r	Radial
ref	Reference
s	Solid (porous matrix)

skin	Skin
τ	Tangential

1. Introduction

Human bodies can be comfortable only in a very limited range of temperatures (Fourt & Hollies 1970). In fact, heat stress is a serious condition that can affect performance or even cause injury (Leithead & Lind 1964). This means that certain situations call for specific types of functional clothing (hereafter referred to as protective clothing) that offer heat and cold protection, such as harsh climates, elite sports practice, or fire-fighting (Rossi 2005; Sobera 2006). Textile design and appropriate materials allow the engineering of adequate garments for such applications, and to do so, it becomes relevant to manufacturers to understand how different parameters can affect the performance of the wearer, in order to select the most suitable construction specifications.

1.1. Scope of the Project

Research in collaboration with EMPA has yielded in the past few years several advances in the topic of transport phenomena between the skin and clothing. Because modelling of flow and heat transfer around a full, moving human body still presents some challenges from a computational cost perspective, initial steps in that direction have included numerical simulation in flat/folded clothing microclimates (Couto & Mayor 2013; Oliveira 2015b) and, to a lesser extent, cylindrical microclimates (Sobera 2006; Oliveira 2015a). This project aims to further contribute to this topic by adding to the latter geometry, a standard test configuration for the protective properties of clothing.

1.2. About EMPA

EMPA is a Swiss research institute located in three different sites: Dubendorf, Thun and St. Gallen. It is as interdisciplinary as it is multicultural, counting with over one thousand staff, researchers and students, who conduct investigations in topics ranging from nanostructured materials to health and performance. Markedly applications-oriented, it is capable of providing its partners with customized solutions and turning research results into marketable innovations. The present study was carried out in the St. Gallen division, particularly in the Laboratory of Protection and Physiology (401).

1.3. Contribution of this Thesis

This thesis contributes to the subject of transport phenomena across clothing microclimates. The geometry and conditions introduced by Oliveira (2015a) in his preliminary report (Figure 3.1) have been studied more extensively, providing hopefully valuable knowledge regarding the influence of both geometrical and physical parameters of the clothing, specifically: air gap thickness ratio (I_g), fabric permeability (expressed by Darcy number, Da), and inner fabric emissivity (ε). The relative importance of heat transfer by natural convection has also been carefully analysed for a variety of conditions.

A comprehensive numerical study of transfer phenomena in air-permeable cylindrical microclimates which accounts for the effects of radiation and natural convection is so far missing in literature.

1.4. Layout of the Thesis

The present work is structured into four main sections: Section 2 - *Context and State of the Art* consists of a brief review of pertinent literature consulted in the duration of this project;

Section 3 - *Background* provides a thorough description of the hardware and software used (3.1), and relevant modelling assumptions and simplifications considered (3.2-3.4, as well as sufficient detail to ensure the reproducibility of this study;

Section 4 - *Results and Discussion* is divided into three subsections. The first concerns the effects of air gap thickness ratio (4.1), and gives an initial description of the flow in the geometry and conditions of this project. Two different approaches were used to study this parameter, each one analysed separately (4.1.1-4.1.2). The influence of the permeability of the fabric (4.2) and of the emissivity of its inner surface (4.3) is likewise investigated;

Section 5 - *Conclusions* gives a short overview of the work done, the key conclusions and recommendations for future work.

2. Context and State of the Art

Numerical simulation approaches to flow and heat transfer problems, unlike purely experimental investigations, offer the clear advantage of being able to produce comprehensive and detailed information, due to the simultaneous computation of different relevant parameters, usually at lower costs. These methods, however, require their reliability to be thoroughly investigated through comparison with published experimental results or benchmark studies (Barry & Hill 2003; Schäfer 2006). Computational Fluid Dynamics (CFD) is one such approach which allows the solving of the multiple model equations involved in transfer phenomena processes such as flow and heat transfer in microclimates between the skin and a piece of fabric for functional clothing applications, as is the aim of this study.

With respect to natural convection, its relevance in engineering applications, such as nuclear energy systems and electronic cooling, has motivated ample numerical and experimental research. Natural convection in rectangular cavities has been studied for different aspect ratios and Rayleigh numbers by Corcione (2003) and for different enclosure inclinations by Soong et al. (1996), who investigated mode-transition and hysteresis phenomena and by Khezzar et al. (2012), who looked into the effect of start-up conditions. Davis (1983) and Ampofo & Karayiannis (2003) provided benchmark numerical and experimental data for natural convection in that geometry for Rayleigh numbers of $10^3 < Ra < 10^6$ and $Ra = 1.58 \times 10^9$, respectively. Furthermore, the coupling of natural convection and radiation for flat setups has been studied by Akiyama & Chong (1997) and, for different inclinations, by Vivek et al. (2012), who concluded that radiation has a significant effect on heat transfer patterns in enclosures. Similarly, transfer problems in cylindrical geometries have received the attention of groups of scientists, namely Stringer et al. (2014), who computed flow around 2D circular cylinders for a range of diameters and flow conditions, Molla et al. (2011), who accounted for radiation and natural convection, and Schäfer & Turek (1996) who provided benchmark computations of laminar flow around 2D and 3D cylinders.

Likewise pertinent to this project is to consider the influence of the permeability of the layer of fabric surrounding the skin on the local flow characteristics and heat fluxes. The modelling of fabric porosity based on material properties has been undertaken by Dunn (2000), and such models can be useful when simulating internal and external fluid flow and heat transfer for enclosures of concentric geometry, as noted before by Sobera (2006). The influence in the flow of a porous outer cylinder around an inner impermeable cylinder falls within the scope of the study of passive flow control around bluff bodies. Numerical studies by Bhattacharyya & Singh (2011), and experimental ones by Ozkan et al. (2012), Ozkan et al. (2013), Gozmen et al. (2013) and Gozmen & Akilli (2014), concluded that the permeable outer layer is efficient in reducing the turbulent kinetic energy and the frequency of vortex shedding at the wake of the inner cylinder.

Particularly, the study of transport phenomena in microclimates between the skin and clothing through CFD includes the work of Sobera (2006) and Sobera & Kleijn (2008), who conducted 3D transient simulations with a Re-Normalization Group $k-\varepsilon$ turbulence model for cylinders surrounded by a porous layer, and the recent contributions of Couto & Mayor (2013) and Oliveira (2015b). The former authors modelled the convective and radiative heat transfer between skin and clothing, while the latter analysed the influence of inclination relative to gravity, external air velocity, air gap thickness, emissivity and thermal resistance of the fabric on the heat and flow patterns for flat geometry enclosures. More recently, Oliveira (2015a) further contributed to this subject by giving the first steps to modelling of the periodic turbulent fluid flow and heat transfer around a sheathed cylinder (2D simulation, concentric geometry, as shown in Figure 3.1) using the Low Reynold's Number $k-\varepsilon$ turbulence model.

This study focuses solely on dry heat transfer phenomena (conduction, convection and radiation) in concentric geometries, a configuration frequently used in the study of heat transfer in protective clothing (Ambesi et al. 2014). As for latent heat and mass transfer phenomena, these are addressed by other authors, namely Barry & Hill (2003), Min et al. (2007), and Murakami et al. (2000).

As described by Sobera (2006), the simulation of transport phenomena in microclimates between the skin and a layer of protective porous clothing, usually follows one of these three different approaches: the micro-, meso- and macro-scale. The micro-scale (sub-millimeter) focuses on finding relationships between fabric geometric properties (e.g. porosity) and hydraulic resistance factors (Angelova et al. 2013; Andrade et al. 1999; Döbrich et al. 2014; Rief et al. 2011; Sobera 2006). As for the meso-scale study (centimeter to decimeter), it aims at modelling velocity, pressure and temperature fields around objects surrounded at some distance by a thin porous layer, particularly the case of an impermeable cylinder surrounded at a fixed distance by a thin layer of clothing, the standard test geometry for measuring the protective performance of garments (Sobera 2006; Oliveira 2015b; Oliveira 2015a). Lastly, the macro-scale approach is similar but uses full-scale 3D human body representations (Sobera 2006; Sobera et al. 2003; Barry & Hill 2003).

3. Background

3.1. Hardware and software

All simulations were carried out in a workstation with two Intel Xeon 2.59 GHz processors, with $48.8\ \mathrm{GB}$ installed RAM. Twenty virtual cores were available, from which each simulation used only four, a number chosen so as to maximize both simulation speed and the ability to run multiple simulations at the same time.

The software selected was COMSOL Multiphysics, version 5.1, due to its capacity to deal with heat transfer by radiation and porous media modelling, a key feature for the present studies.

3.2. Geometry and boundary/initial conditions

The configuration used throughout this study consists of a two-dimensional (2D) representation of a horizontal impermeable cylinder (skin), surrounded at a varying distance by a layer of porous material (fabric). A circular external domain was used, similarly to what was done by Breuer (1998) and Breuer (2000), in order to avoid the possible influence of the proximity of the walls on the flow around the clothed limb. This decision could, however, be reassessed if a more efficient mesh selection was to be achieved.

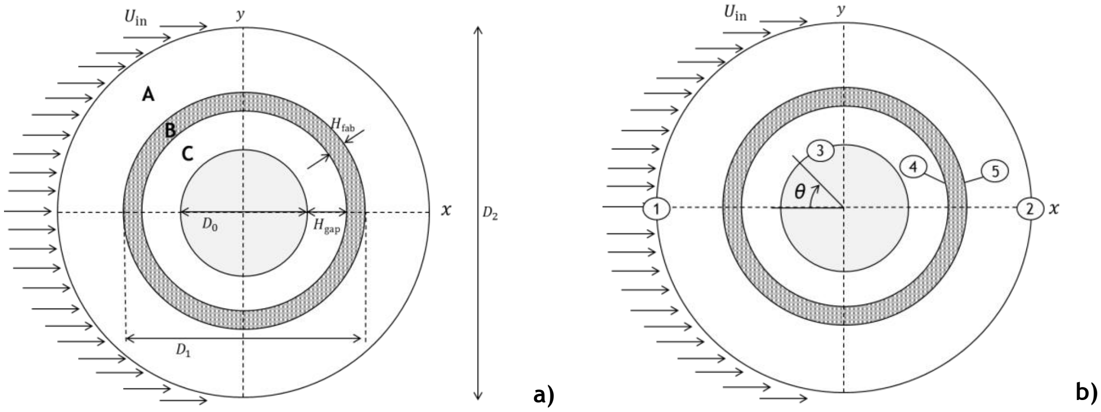

Figure 3.1: Geometry used in the study: a) schematic representation of the distances within the geometry; b) boundary indexes (1-5). Letters A, B and C represent the external, fabric and microclimate domains, respectively. Drawings are not to scale.

The diameter of the limb was fixed at $D_0 = 0.10\ \mathrm{m}$, except in Section 4.1.2, and fabric thickness at $H_{\text{fab}} = 0.562\ \mathrm{mm}$. The thickness of the air gap (H_{gap}) was calculated so as to obtain the specified ratios of air gap thickness to outer fabric diameter ($I_\mathrm{g} = H_\mathrm{gap}/D_1$). Outer fabric diameter varied according with the air gap thickness ($D_1 = D_0 + 2H_\mathrm{gap} + 2H_\mathrm{fab}$), again with the exception of Section 4.1.2, where it was kept constant at $0.11\ \mathrm{m}$. Diameter of the external domain, D_2, was chosen as $30 \times D_1$, as used previously by Oliveira (2015a).

Boundary conditions were obtained from the work of Sobera & Kleijn (2008) and are presented in Table 3.1. The limb surface and the outer fabric (boundaries 3 and 5, Figure 3.1b) were attributed emissivities of 0.95 and 0.77, respectively, while the emissivity of the inner fabric was a varying parameter. Inlet velocity U_in was calculated in each simulation case using fluid properties from Table 3.2 in order to keep Reynolds number constant at 3900 ($Re = \rho U_\mathrm{in} D_1/\mu$), corresponding to $0.54\ \mathrm{m/s}$ for an external (fabric) diameter of $0.11\ \mathrm{m}$.

Table 3.1: Boundary conditions.

Boundaries	Fluid flow boundary conditions	Heat transfer boundary conditions
1 (inlet)	Uniform inlet velocity: $u = U_\mathrm{in}$; $v = 0$ Turbulence intensity (I) and length scale (L_T): $I = 0.05$; $L_\mathrm{T} = 0.08 \times D_1$	Constant temperature: $T_\mathrm{c} = 283.15\ \mathrm{K}$
2 (outlet)	Pressure outlet with backflow: Gauge $p = 0\ \mathrm{Pa}$	Outflow
3 (limb wall)	Wall, no-slip condition	Constant temperature: $T_\mathrm{h} = 309.15\ \mathrm{K}$ $\varepsilon = 0.95$
4 (inner side of the porous layer)	No constraints	$\varepsilon = \varepsilon_\mathrm{inner\ fabric}$
5 (outer side of the porous layer)	Pressure outlet with backflow: Absolute pressure $= p + 1\ \mathrm{atm}$	$\varepsilon = 0.77$

Solutions were initialized with null values for each velocity component as well as for pressure. In order to improve convergence, a step function was introduced at $t = 0.1\ \mathrm{s}$ so that velocity varies smoothly from practically zero to U_in. Temperatures were initialized on the external domain (domain A) with the ambient air temperature, T_air; on the fabric and microclimate, initial temperatures were set to T_skin, corresponding to the temperature of the skin.

3.3. General assumptions and mathematical models

Studies were carried out considering constant physical fluid (air) properties and using arithmetic average temperature values when estimating air properties, as shown in equation 1 (Çengel 2002, p.371).

$$\frac{T_{\mathrm{skin}} + T_{\mathrm{air}}}{2} \tag{1}$$

where T_{skin} and T_{air} represent the skin and external air temperatures, respectively. The fluid was considered Newtonian (i.e. its viscosity is independent of the shear rate applied) and incompressible, as the pressure should not vary by more than $20\ \%$ and air velocity is lower than $30\ \%$ the velocity of sound (i.e. $Ma < 0.3$) (Coulson & Richardson 1999, p.143; COMSOL 2015). Fluid properties used for each of the studies are shown in Table 3.2, and were obtained from polynomial functions used by Shi et al. (2004), as shown in equation 2, where ϕ_{f} is any given fluid property and a_0, a_1 and a_2 are coefficients.

$$\phi_{\mathrm{f}} = a_0 + a_1 T + a_2 T^2 \tag{2}$$

Table 3.2: Properties of the air.

Property	Units	Value
$\mathbf{C_{p,f}}$	$\mathrm{J/(kg\,K)}$	1.0068×10^4
$\boldsymbol{k_{\mathrm{f}}}$	$\mathrm{W/(m\,K)}$	2.5908×10^{-2}
$\boldsymbol{\rho}$	$\mathrm{kg/m^3}$	1.1785
$\boldsymbol{\mu}$	$\mathrm{Pa\,s}$	1.8380×10^{-5}
$\boldsymbol{\beta}$	$\mathrm{1/K}$	3.3767×10^{-3}

Properties of the solid matrix within the fabric (domain B) can be found in Table 3.3, considering cotton as the material. Specific heat for cotton $C_{\mathrm{p,s}}$ was taken from Incropera et al. (2007, p.939), and thermal conductivity k_{s} was calculated so as to maintain the thermal resistance of the fabric (R_{CT}, see Appendix G for formula) constant, along with a porosity $\gamma = 0.7$ (Dhinakaran & Ponmozhi 2011). Cotton density ρ_{s} was obtained from International Fibre Centre (2004). Effective properties of the fabric (ϕ_{fab}) are calculated by the software using:

$$\phi_{\mathrm{fab}} = \gamma\phi_{\mathrm{f}} + (1-\gamma)\phi_s \tag{3}$$

Table 3.3: Properties of the solid matrix in the fabric layer (domain B).

Property	Units	Value
$C_{\mathrm{p,s}}$	$\mathrm{J/(kg\,K)}$	1.300×10^3
k_{s}	$\mathrm{W/(m\,K)}$	Variable: $k_{\mathrm{s}} = \left[\frac{D_0 \ln\left(1+\frac{H_{\mathrm{fab}}}{D_0/2+H_{\mathrm{gap}}}\right)}{2\,R_{\mathrm{CT}}} - \gamma\, k_{\mathrm{f}}\right]/(1-\gamma)$
ρ_{s}	$\mathrm{kg/m^3}$	1.500×10^3

Two-dimensional simulations were performed, assuming that the effect of the third dimension is negligible. Simulations were carried out in transient state, to account for the time periodicity of the flow (Çengel 2002, p.382). As $Re = 3900$, a turbulence model had to be included, in this case the Low-Reynolds Number $k-\varepsilon$ (hereafter referred to as LRN). This model is one among those available in the chosen CFD software for this project (COMSOL Multiphysics), and was proven to be the most suitable for this study (for a comparison with the Shear Stress Transport turbulence model, see Appendix E).

The sheathed cylinder had three main flow domains: the external domain (A) was modelled using the turbulence model described above, and the internal (C) and the fabric domains (B) where laminar regime was assumed, given the much lower velocities expected in the microclimate and fabric (Sobera 2006).

The continuity equation (mass conservation equation) can be written as follows:

$$\nabla \cdot \vec{U} = 0 \tag{4}$$

with $\vec{U}$ being the velocity magnitude vector. Three different momentum equations must be defined, one for each of the domains (Figure 3.1), where ρ is the density, p the pressure, μ the dynamic viscosity, T the temperature, and t the time (equations 5-7). $\vec{F}$ is the force vector, considered null for cases where natural convection was neglected, or given by equation 8 when it was considered.

$$\text{A:} \quad \rho \cdot \frac{\partial \vec{U}}{\partial t} + \rho \cdot (\nabla \cdot \vec{U})\vec{U} = \nabla \cdot \left(-p + (\mu + \mu_T)\left(\nabla \vec{U} + (\nabla\vec{U})^T\right) - \frac{2}{3}\rho k\right) + \vec{F} \tag{5}$$

B: $$\frac{\rho}{\gamma}\cdot\left(\frac{\partial\vec{U}}{\partial t}+\rho\cdot\left(\nabla\cdot\vec{U}\right)\frac{\vec{U}}{\gamma}\right)=\nabla\cdot\left(-p+\frac{\mu}{\gamma}\left(\nabla\vec{U}+\left(\nabla\vec{U}\right)^{T}\right)-\frac{2\mu}{3\gamma}\left(\nabla\cdot\vec{U}\right)\right)-\frac{\mu}{K}\vec{U}+\vec{F} \tag{6}$$

C: $$\rho\cdot\frac{\partial\vec{U}}{\partial t}+\rho\left(\nabla\cdot\vec{U}\right)\vec{U}=\nabla\cdot\left(-p+\mu\left(\nabla\vec{U}+\left(\nabla\vec{U}\right)^{T}\right)\right)+\vec{F} \tag{7}$$

$$\vec{F}=(\rho-\rho_{\mathrm{ref}})\vec{g}\approx-\rho_{\mathrm{ref}}\beta(T-T_{\mathrm{c}})\vec{g} \tag{8}$$

In the latter equation, $\vec{F}$ corresponds to the buoyancy force as given by the Boussinesq approximation, which assumes that the variations in density can be considered negligible except where they are multiplied by $\vec{g}$, the gravitational acceleration. Such approximation enables an approach to buoyant flows without having to consider the more complicated Navier-Stokes equations for compressible flow, and is valid for this particular case because $\Delta\rho/\rho_{ref} \ll 1$ (COMSOL 2015, p.107).

Domain B corresponds to the fabric, a porous region where pressure drop ΔP may be described as a function of permeability K by Darcy's law (Dunn 2000):

$$\frac{\Delta p}{H_{\mathrm{fab}}}=\frac{\mu}{K}\vec{U} \tag{9}$$

Flow is non-isothermal, so an energy equation must be added, written as follows:

$$\rho C_{\mathrm{p}}\frac{\partial T}{\partial t}+\rho C_{\mathrm{p}}\vec{U}\cdot\nabla T=\nabla\cdot(k\,\nabla T) \tag{10}$$

where C_{p} is the specific heat. Turbulent flow in the external domain was accounted for by the LRN $k-\varepsilon$ model, described by equations 11-19 (COMSOL 2015, p.158). Please note that, unlike everywhere else in this document, ε stands for the turbulent dissipation rate and f_{ε}, f_{μ} are functions in the turbulence model.

$$\rho\cdot\frac{\partial TKE}{\partial t}+\rho\vec{U}\cdot\nabla TKE=\nabla\cdot\left(\left(\mu+\frac{\mu_{\mathrm{T}}}{\sigma_{\mathrm{k}}}\right)\nabla TKE\right)+P_{k}-\rho\varepsilon \tag{11}$$

$$\rho\cdot\frac{\partial\varepsilon}{\partial t}+\rho\vec{U}\cdot\nabla\varepsilon=\nabla\cdot\left(\left(\mu+\frac{\mu_{\mathrm{T}}}{\sigma_{\varepsilon}}\right)\nabla\varepsilon\right)+\mathrm{C}_{\varepsilon1}\frac{\varepsilon}{TKE}P_{\mathrm{k}}-\mathrm{C}_{\varepsilon2}\rho\frac{\varepsilon}{TKE}f_{\varepsilon} \tag{12}$$

$$P_{\mathrm{k}}=\mu_{\mathrm{T}}\left(\nabla\vec{U}:\left(\nabla\vec{U}+\left(\nabla\vec{U}\right)^{\mathrm{T}}\right)-\frac{2}{3}\left(\nabla\cdot\vec{U}\right)^{2}\right)-\frac{2}{3}\rho\,TKE\,\nabla\cdot\vec{U} \tag{13}$$

$$\mu_{\mathrm{T}} = \rho C_{\mu} \frac{TKE^2}{\varepsilon} f_{\mu} \tag{14}$$

$$f_{\mu} = (1 - \mathrm{e}^{-\mathrm{l}^*/14})^2 \cdot \left(1 + \frac{5}{R_{\mathrm{t}}^{\frac{3}{4}}} \mathrm{e}^{(R_{\mathrm{t}}/200)^2}\right) \tag{15}$$

$$f_{\varepsilon} = (1 - \mathrm{e}^{-\mathrm{l}^*/3.1})^2 \cdot (1 - 0.3\mathrm{e}^{(R_{\mathrm{t}}/6.5)^2}) \tag{16}$$

$$l^* = (\rho u_{\varepsilon} l_{\mathrm{w}})/\mu \tag{17}$$

$$R_{\mathrm{t}} = \rho\, TKE^2/(\mu\varepsilon) \tag{18}$$

$$u_{\varepsilon} = (\mu\varepsilon/\rho)^{1/4} \tag{19}$$

In the above equations, $C_{\varepsilon 1}$, $C_{\varepsilon 2}$, C_{μ}, σ_k and σ_{ε} are turbulence model parameters, kept as default in this work as 1.5, 1.9, 0.09, 1.4 and 1.5, respectively; l_{w} is the distance to the closest wall.

Heat transfer by radiation was included by selecting boundaries 3, 4 and 5 as participating surfaces for surface-to-surface radiation. Each boundary was given a constant emissivity, with values as presented in Table 3.1. Ambient temperature was set to $283.15\ \mathrm{K}$, the temperature of ambient air.

3.4. Simulation settings

Meshes used in this study were hybrid, with $38'038$ grid elements, except for cases with air gap ratio $I_{\mathrm{g}} > 0.05$ (refer to Appendix A for details). A mesh independence study was performed prior to the parametric analysis, by comparing flow and heat transfer results between three increasingly refined meshes. The mesh was then chosen in an effort to reach an acceptable compromise between computational costs (simulation time and memory) and accuracy of the results (see Appendix D).

A total of $150\ \mathrm{s}$ of flow were simulated, as this was found to be the time required to reach a periodic behaviour of flow and heat transfer variables.

Regarding the solver's time stepping, the Backward Differentiation method was used, as default in COMSOL, where all settings were also kept as default except for the maximum time step, which was changed to $0.1\, D_1/U_{\mathrm{in}}$, the same as Sobera & Kleijn (2008). This was chosen in order to guarantee that the solver time step was not higher than the time it takes for a fluid element to move a distance of one tenth of the clothed limb diameter, this way capturing the time oscillations of the flow. Concerning data-saving time stepping, a $0.01\ \mathrm{s}$ time step was used for the interval $t = [120{,}150]\ \mathrm{s}$ since this was found to provide enough data points per vortex shedding period. To save on computation time and file size, data was saved only every $10\ \mathrm{s}$ for $t = [0{,}100]\ \mathrm{s}$ and $1\ \mathrm{s}$ for $t = [100{,}120]\ \mathrm{s}$.

Results were time-averaged over one vortex shedding period for $t \geq t_0$, with t_0 being the flow time from which variables become time-periodic. For this purpose a script in MATLAB Livelink was used, which calculates t_0 and the frequency of vortex shedding, f, by analysing the evolution of transverse velocity v/U_{in} over time. The mentioned script was further developed to perform most of the post processing of the results automatically.

The criteria for convergence used were an absolute tolerance of 10^{-5} for pressure, velocity, and temperature, an unscaled tolerance of 10^{-4} for turbulent kinetic energy (TKE) and 8×10^{-4} for the turbulent dissipation rate, ε.

4. Results and Discussion

A thorough description and analysis of the parametric studies conducted in this project is presented in this section. Specifically, the following subsections will include the results concerning the influence of heat transfer phenomena such as radiant exchange and natural and forced convection, as well as the parameters air gap thickness to outer diameter ratio, fabric permeability, and inner fabric emissivity. Relevant physical and geometrical properties considered in each study can be found in detail in Appendix B. Mass and energy imbalances were calculated according to the equations displayed in Appendix G, and are made available in Appendix C.

Validation of the computational methods was conducted by comparing the results obtained using the current flow and heat transfer models with published results (Sobera & Kleijn 2008; Sobera et al. 2003; Sobera 2006), which can be found in Appendix D.

4.1. Influence of the Air Gap Thickness Ratio (I_g)

Dimensionless parameter I_{g}, representing the ratio of air gap thickness to outer fabric diameter (H_{gap}/D_1), was varied from 0.05 to 0.25, values that correspond to air gaps of $6\ \mathrm{mm}$ or $51\ \mathrm{mm}$, respectively. These values are representative of the low- and high-end of the range of air gap thicknesses observed in clothing (Psikuta et al. 2012). Parameter I_{g} was chosen instead of the more commonly used H_{gap}, for an easier comparison with the reference work of Sobera (2006), and because of its relevance to the transport processes occurring in the microclimate. Throughout this study, permeability of the fabric, as given by the dimensionless Darcy number, was fixed at 2×10^{-3}, and Reynolds number was kept constant at 3900.

The study of the effects of parameter I_{g} was the one posing most practical difficulties from an implementation point of view. This is because, when keeping the diameter of the limb (D_0) and the inlet velocity of air (U_{in}) constant (as performed in Sections 4.2 and 4.3), an increase in I_{g} directly implies an increase in outer diameter (D_1) and in Reynolds number (Re). Significantly altering Re is not desirable, since it may be accompanied by a different suitability of the numerical models used, namely turbulence model Low-Reynolds number $k - \varepsilon$, which cannot be quantified without a proper validation against numerical or experimental flow and heat transfer data, at those Re. This was not possible, both because such complete data are not available for all Re, and because doing so would require strenuous computational effort in a time span that was not compatible with this master's thesis. Two other strategies were available, where Re could be kept constant at 3900: **1)** Keeping the <u>diameter of the limb constant</u> at $0.10\ \mathrm{m}$, increase I_g by increasing the diameter of the outer fabric. Re can be maintained at 3900 by decreasing the inlet air velocity (Figure 4.1a). This approach has the disadvantage of altering the air velocity entering the microclimate. Therefore, the flow and heat flux changes that are observed when I_g is increased are not only due to the effect of the larger air gap, but also, to some extent, to the lower inlet velocity that is imposed. **2)** Keeping the <u>diameter of the outer fabric constant</u> at $0.11\ \mathrm{m}$, increase I_g by decreasing the diameter of the limb (Figure 4.1b). Re is thus maintained at 3900 because the outer diameter does not change. This method was the one chosen by Sobera (2006), and it allows the velocity to be kept constant while I_g varies. However, as the size of the limb changes, the amount of heat power that reaches the microclimate is not the same, and neither is the flow around the limb.

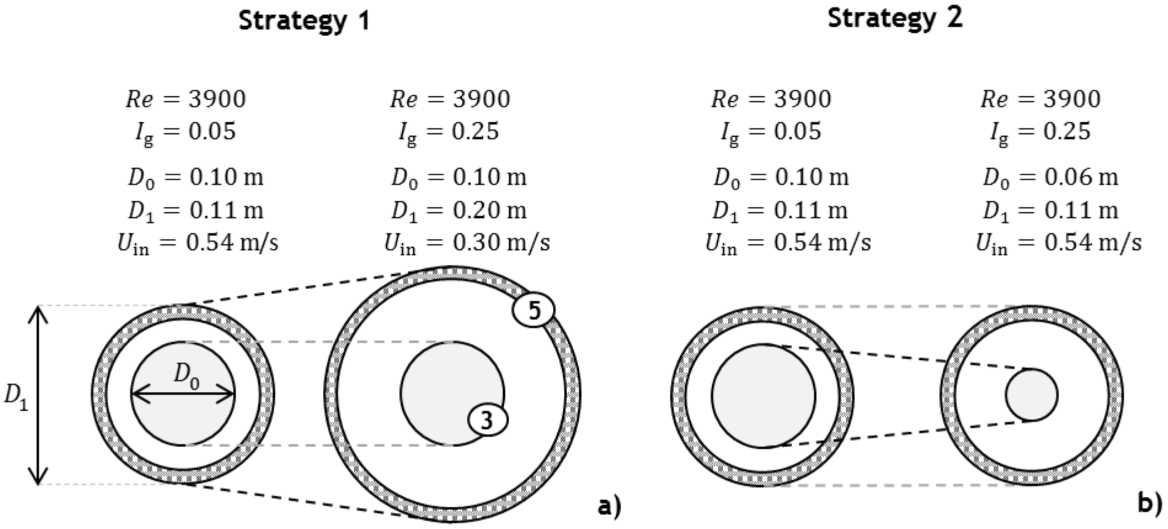

Figure 4.1: Schematic representation of the two approaches followed when studying the effects of varying the air gap thickness ratio (I_g). Drawings are not to scale.

Two subsections within Section 4.1 were created, where the two above described strategies are tested and discussed. The results hereby presented aim to provide information that allows for an assessment of the relative importance of natural convection, along with an approximate prediction of the threshold of I_g over or under which this heat transfer phenomena can no longer be ignored (Section 4.1.1). They also aim to allow some conclusions regarding the influence of varying air gap thickness ratios on the flow and especially on the heat transferred in the microclimate around the skin (Section 4.1.1 and 4.1.2). A brief analysis of the flow behaviour in horizontal microclimates with concentric geometry is also presented (Section 4.1.1).

4.1.1. Strategy 1: constant diameter of the limb ($\boldsymbol{D_0}$)

In this subsection, three different I_{g} were simulated (0.05, 0.10 and 0.25), for two extreme values of inner fabric emissivity ε (0.05 and 0.95), for cases where natural convection was either ignored or considered. This was accomplished by successively increasing D_1, which means the flow characteristic length also increases.

In order to keep Reynolds number ($Re = \rho U_{\mathrm{in}} D_1/\mu$) constant at 3900, the inlet velocity (U_{in}) was decreased (Figure 4.1a). When following this strategy, to compare the lowest I_{g} (0.05) to the highest (0.25) corresponds to comparing air flow and heat transfer around a thin limb (e.g. an upper arm) with a small air gap thickness ($6\ \mathrm{mm}$) and a given inlet air velocity ($0.54\ \mathrm{m/s}$), to air flow and heat transfer around the same limb but with a high air gap thickness ($51\ \mathrm{mm}$) and a lower inlet air velocity ($0.30\ \mathrm{m/s}$). The intermediate I_{g} (0.10) corresponds to an intermediate air gap thickness ($13\ \mathrm{mm}$) and intermediate inlet velocity ($0.48\ \mathrm{m/s}$). While aware that this approach is not fully representative of a real-life situation, because U_{in} does not remain constant, still some meaningful conclusions can be drawn, particularly regarding the importance of natural convection.

An average time of $54\ \mathrm{h}$ was needed to complete each simulation case, from a total of twelve cases. Memory requirements fell within a maximum of $3.7\ \mathrm{GB}$, mass imbalances were kept below $0.1\ \%$, and energy imbalances at the microclimate below $1\ \%$, while energy imbalances at the fabric varied from less than $1\ \%$ to over $25\ \%$. Imbalances were observed to be highest for the cases with the highest I_{g}, which could indicate that the grid chosen for those cases may not be adequate. Given that these imbalances are in some cases well above what would generally be considered acceptable, a more thorough analysis and discussion of the obtained mass and energy imbalances can be found in Appendix C, which was excluded from the main text for the sake of clarity and conciseness.

Figure 4.2 displays the velocity map with velocity vectors indicative of the direction of the flow, and the same velocity map but with streamlines, for the case where $I_{\mathrm{g}} = 0.25$ and $\varepsilon = 0.95$. Instantaneous velocity maps, obtained for four sequential times during one vortex shedding period, are shown in Figure 4.3. Figure 4.4 shows the time-averaged velocity and temperature maps obtained for each test case and Figure 4.5 the time-averaged radial velocity. Figure 4.6 illustrates the results for total, convective and radiative heat fluxes around the skin (boundary 3, Figure 3.1b). Time-averaged temperature of the outer fabric is shown in Figure 4.7. Lastly, results for time- and space-averaged heat losses around the skin are displayed in Figure 4.8.

For some values of I_g, e.g. $I_g = 0.25$ and $\varepsilon = 0.95$, flow and temperature patterns are observed to be significantly different when natural convection is neglected, as compared to when it is considered, which indicates that the influence of natural convection is not negligible (Figure 4.4w and 4.4x, compared to 4.4k and 4.4l). When natural convection is considered, two counter-rotating convection cells form within the microclimate, one at either side of the limb (Figure 4.2). On both cells, ascending flow occurs near the skin, while descending flow occurs near the fabric (Figure 4.2a). The convection cell located at the upstream side (quadrants I/IV) is characterized by higher descending air velocities than those observed at the downstream cell. This is because, upstream, cool air (denser) is permeating to the microclimate and joining the descending air current, due to the prevalence of buoyancy forces over inertia forces. Curiously, it was found that even some of the air entering the microclimate at $\theta > 0°$ followed this downwards trajectory (Figure 4.2b), again signalling the importance of natural convection. Some fluid elements then rise when they come close to the skin, as their temperature increases and they become less dense, leaving the microclimate at a y-coordinate above where they had entered.

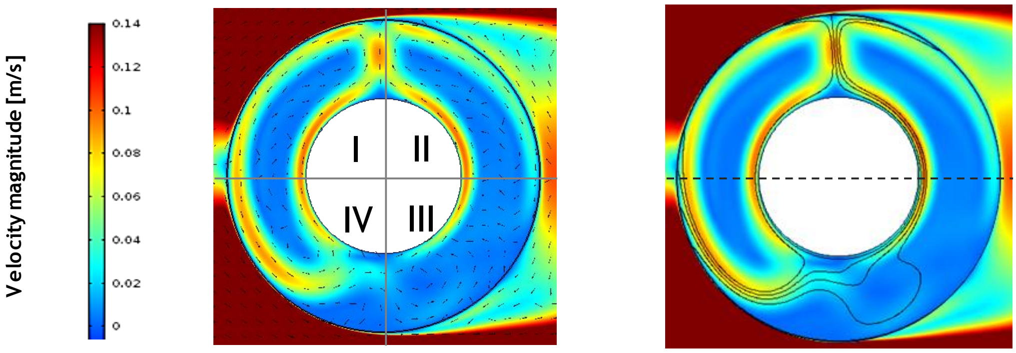

a) b)

Figure 4.2: Time-averaged velocity magnitude map with velocity vectors (a) and velocity magnitude map with streamlines (b) inside and outside the clothing layer, for air gap thickness ratio $I_g = 0.25$ and inner fabric emissivity $\varepsilon = 0.95$, where the effects of natural convection are considered. A colour legend can be found at the left.

External air flow downstream of the clothed limb is turbulent ($Re = 3900$), and characterized by periodic vortex shedding downstream of the clothed limb. Flow separation, defined as the detachment of the velocity boundary layer from the surface (White 2011) and corresponding to null shear stress, occurs at $\theta \sim 90°$ and $\theta \sim 260°$ (quadrants II/III; Figure 4.3). One vortex is shed every half period[1], alternatively near the upper and lower separation points, forming a Kármán vortex street downstream.

---

[1] The vortex shedding frequency f was obtained using a script in Matlab, which calculates the amount of time that is needed for the transverse velocity at a point in the centreline ($x/D_1 = 3$) to reach zero thrice.

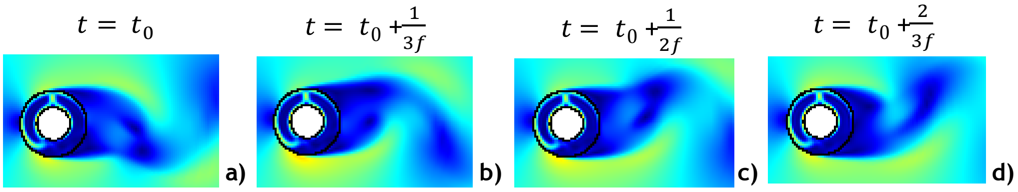

Figure 4.3: Instantaneous velocity maps obtained for four sequential times, during one vortex shedding period ($1/f$). The colour legend is identical to the one in Figure 4.4.

The analysis of time-averaged velocity and temperature maps (Figure 4.4) is a simple yet valuable way of generally understanding how the flow and heat transfer in the enclosure between the skin and the layer of fabric can be affected by modifying a physical or geometrical parameter of the clothing, in this case the thickness of the air gap. A quick look at these maps makes it clear that, for $I_g > 0.10$, there are significant differences between considering or neglecting natural convection (Figure 4.4m-x, as compared to 4.4a-l), to the point where excluding this phenomenon from the heat transfer models could cause problematic over- or under-predictions of the heat fluxes. Also, increasing the air gap thickness ratio seems to heighten the differences between considering or neglecting natural convection, as seen for the highest I_g (0.25), for which two convection cells are formed in the microclimate when natural convection is considered, whereas no such behaviour is observed when it is ignored (Figure 4.4w, compared to 4.4k. For the lowest I_g (0.05), both scenarios yield very similar velocity and temperature maps, i.e. practically symmetrical with respect to $y = 0$ (Figure 4.4o, compared to 4.4c), indicating that natural convection is probably not important for that I_g.

The temperature map (Figure 4.4x) illustrates the effects of the existence of convection currents, as the highest temperatures are observed in the upper regions (quadrants I/II), and the lowest temperatures in the lower regions (quadrants III/IV). The thermal boundary layer is the thinnest in the lower regions, and increases when moving to the upper regions, where an ascending thermal plume is formed, in agreement with literature for natural convection around horizontal cylinders (Çengel 2002, p.469).

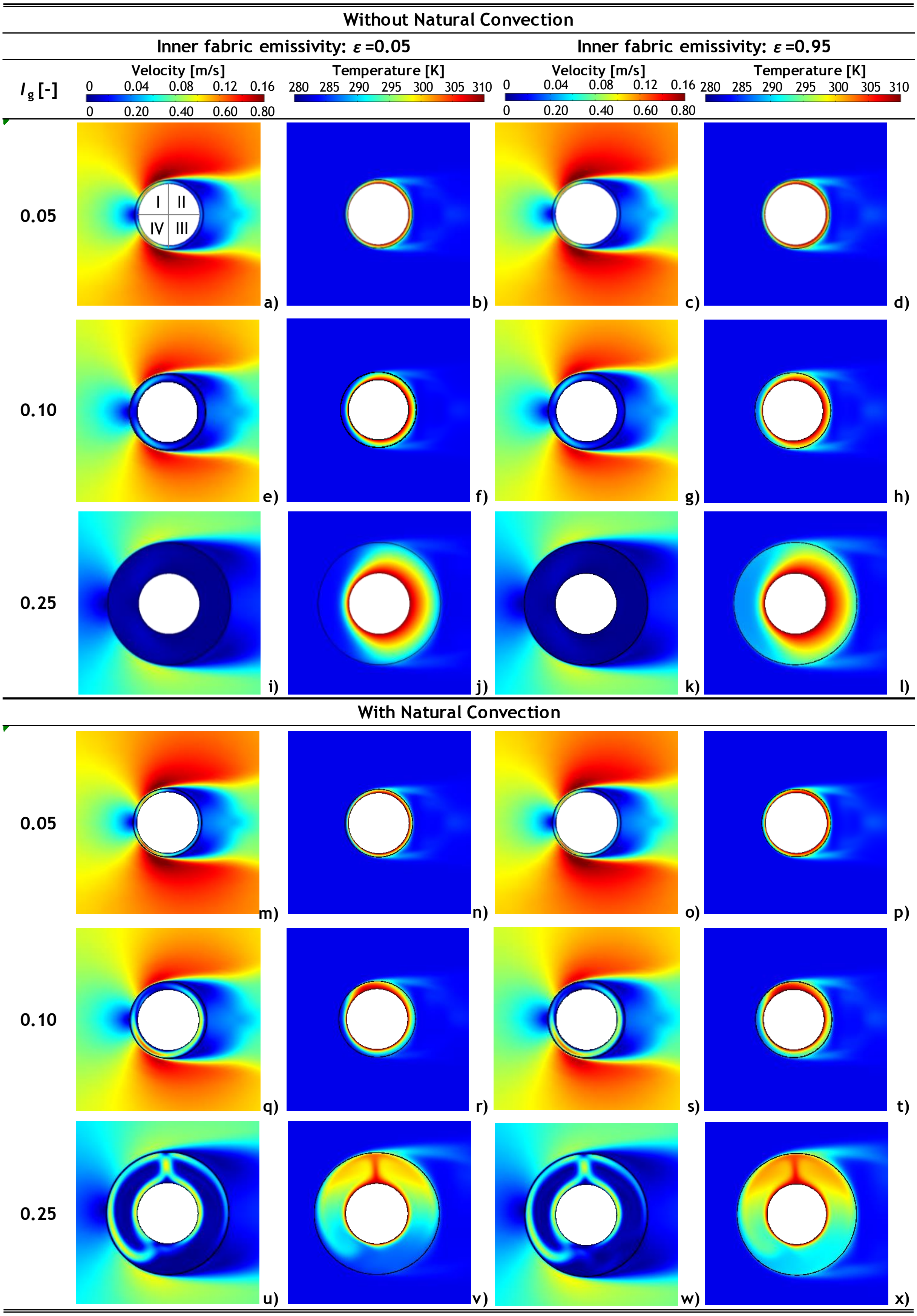

Figure 4.4: Time-averaged velocity magnitude (first and third columns) and temperature (second and fourth columns) maps in the air gap and vicinities for three different air gap thickness ratios (0.05, 0.10 and 0.25) and two inner fabric emissivities (0.05 and 0.95), for cases where natural convection is either ignored (a-l) or considered (m-x). Colour legends can be found on top of each column; in the velocity legend, the values above it are valid for the regions inside the microclimate, and the ones below are valid outside the microclimate.

Contrarily to intuition, this thermal plume is located slightly off-centre, tilted towards the upstream side ($\theta \sim 87°$). This is probably because the outer fabric temperatures are a little lower upstream (quadrant I) than downstream (quadrant II; e.g. Figure 4.7b, full black line).

Further examination of the time-averaged velocity and temperature maps for the cases where natural convection is neglected (Figure 4.4a-l) shows that velocity and temperature are symmetrical between the upper and lower regions of the microclimate (quadrants I/II and III/IV, respectively), as expected given that the temperature field is not coupled to the flow field through the buoyancy forces. Increasing I_g is seen to result in lower velocities both within the microclimate and in the external domain (Figure 4.4c, 4.4g and 4.4k), although it is not yet clear whether this is due to the increase of I_g or to the reduction of the inlet velocity, as will be discussed throughout this section. Moreover, an increase in I_g (and a reduction of the inlet air velocity) causes the thermal boundary layer close to the skin to thicken, especially in the downstream regions (quadrants II/III; Figure 4.4d, 4.4h and 4.4l).

Now, when natural convection is duly considered (Figure 4.4m-x), the interpretation becomes much less straightforward. Raising I_g from 0.05 to 0.25 causes the flow pattern to increase in complexity, from a situation where it is practically symmetrical between the upper and lower regions of the enclosure, to where not only there is no symmetry, but also where convection cells exist (Figure 4.4o-p, compared to 4.4w-x). The thermal boundary layer seems to become thicker for the highest I_g (0.25), except in quadrant III, where it appears to become thinner (even though part of this effect may be due to a lower inlet velocity). The intermediate I_g (0.10) corresponds to an intermediate state, where buoyancy forces are non-negligible, as proved by the already asymmetrical velocity and temperature patterns, but where there is still not enough space for convection cells to develop (Figure 4.4s-t).

Raising the emissivity of the inner fabric from 0.05 to 0.95 seems to have only a small effect on the flow pattern, judging from the similar velocity maps for both situations (e.g. Figure 4.4m, compared to 4.4o). Regarding the temperature, however, results show that a higher ε causes temperatures in the microclimate to be generally higher, and the thermal boundary to be thicker (e.g. Figure 4.4n, compared to 4.4p).

Since the influence of having lowered the inlet air velocity with increasing I_g (in order to keep Re constant at 3900) is not yet fully understood, it can be useful to look at the variation of the results of dimensionless velocity $U_\mathrm{r}/U_\mathrm{in}$ around the outer fabric (Figure 4.5). When natural convection is neglected, by comparing results obtained for a lower I_g (0.05) with those for a higher I_g (0.25), one observes that the velocity magnitudes decrease with increasing I_g (Figure 4.5, dashed black line, compared to dashed blue line). This behaviour is counterintuitive, given that a higher I_g implies a larger microclimate, so the pressure within it was predicted to be overall lower, and the pressure gradient between the inside and outside of the microclimate to be higher, thereby increasing the velocity of air permeating the fabric. These contradictory results create an obvious complexity in the analysis of the effects of increasing I_g on flow and heat transfer, as it becomes unclear if lower heat fluxes are due to the more isolating nature of a larger microclimate, or rather to the lower inlet velocities that were imposed. For that reason, conclusions regarding the influence of I_g will be deferred until the next subsection (Section 4.1.2, where inlet velocities are kept constant). It is possible, nonetheless, to draw conclusions regarding the importance of natural convection, since the comparison between cases neglecting or considering natural convection for a given I_g is still valid (inlet velocity does not change).

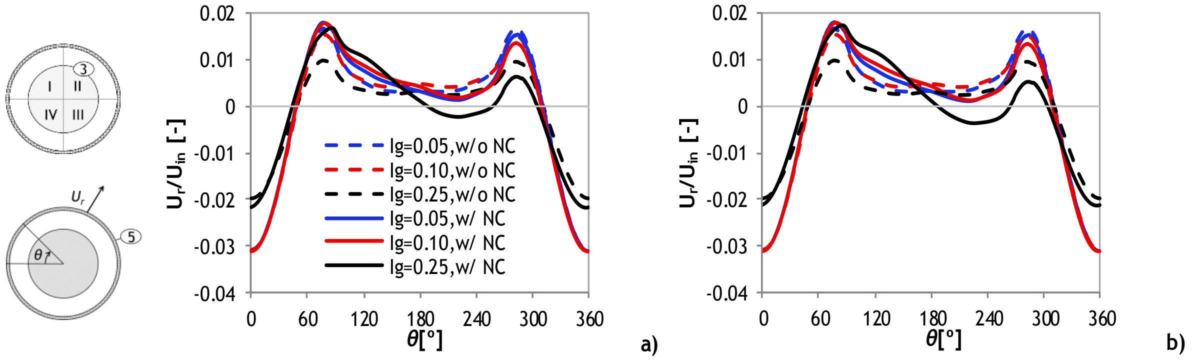

Figure 4.5: Time-averaged radial velocity at the outer fabric (boundary 5) vs angular position: a) $\varepsilon = 0.05$; b) $\varepsilon = 0.95$. Negative velocities mean that air is entering through the fabric. Legend: NC-natural convection.

Heat fluxes at the skin are shown to be significantly different when neglecting or considering natural convection (Figure 4.6, dashed lines, compared to full lines). Neglecting natural convection meant that the results obtained regarding the heat fluxes at the skin were symmetrical between the upper and lower regions (quadrants I/II and III/IV, respectively). This was expected, since the buoyancy forces that are responsible for making the flow and heat transfer asymmetrical are not considered.

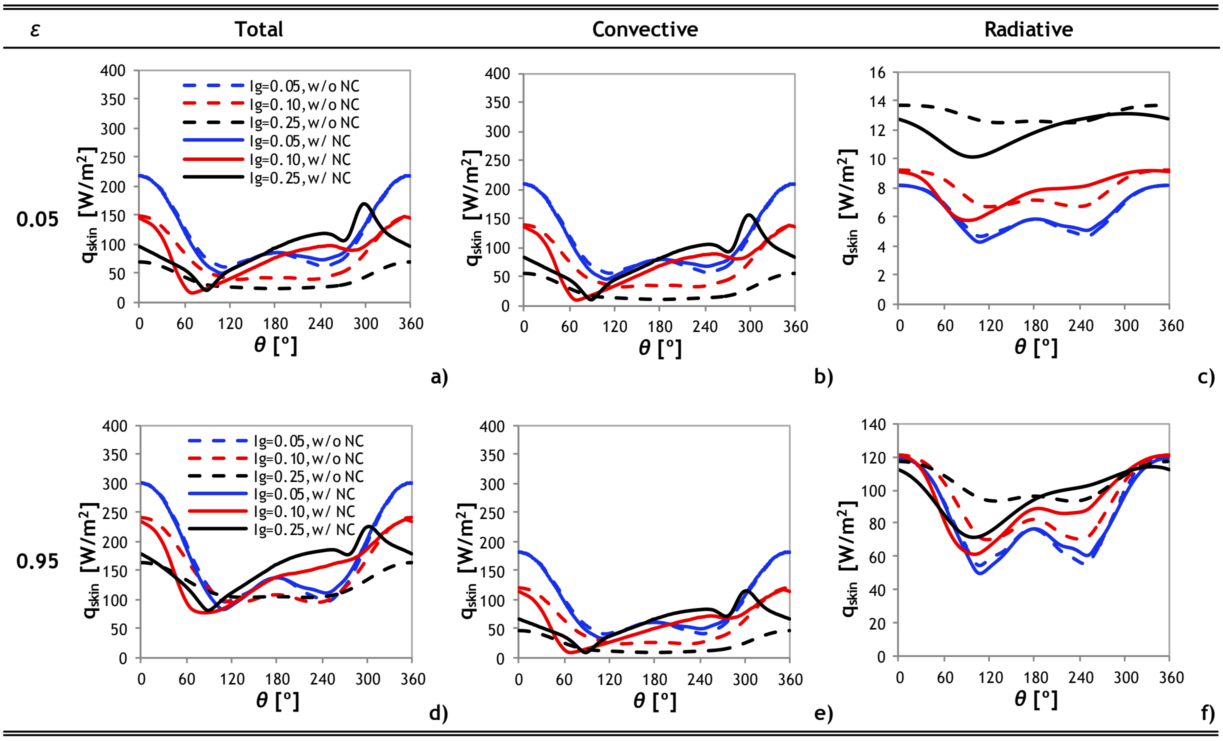

Figure 4.6: Time-averaged total, convective and radiative (a,d; b,e; c,f, respectively) heat fluxes at the skin (boundary 3, Figure 3.1b), evaluated for three different air gap thickness ratios (0.05, 0.10 and 0.25) and two different inner fabric emissivities (0.05 and 0.95), for cases where natural convection is neglected or considered. Legend: NC-natural convection.

When natural convection is considered, time-averaged heat fluxes around the skin are asymmetrical (Figure 4.6, full lines). This is because the cooler (denser) fluid elements tend to descend to the lower regions, and the warmer (less dense) fluid elements to ascend to the upper regions, therefore causing the temperature and the thermal boundary layer to be uneven around that surface (e.g. Figure 4.4x). The local heat fluxes at the skin also show that natural convection plays an increasingly important role with increasing I_{g}, as proved by the progressively higher discrepancies between considering and neglecting this phenomenon (Figure 4.6, full lines compared to dashed lines). In fact, it is observed that for the lowest I_{g} (0.05), there is practically no difference between considering or ignoring natural convection (Figure 4.6a and 4.6d, full blue line compared to dashed blue line), with disagreements corresponding to less than $10\ \%$ in most regions, except at $80° < \theta < 120°$ and $220° < \theta < 280°$, where these reach a maximum of $24\ \%$ or $17\ \%$ ($\varepsilon = 0.05$ or $\varepsilon = 0.95$, respectively). For the highest I_{g} (0.25), however, ignoring natural convection meant that total heat fluxes are underestimated by up to $28\ \%$ or $8\ \%$ ($\varepsilon = 0.05$ or $\varepsilon = 0.95$) for $0° < \theta < 80°$, and up to $76\ \%$ or $41\ \%$ ($\varepsilon = 0.05$ or $\varepsilon = 0.95$) for $100° < \theta < 360°$. At $80° < \theta < 100°$, total heat fluxes at the skin are overestimated by up to $48\ \%$ or $41\ \%$ ($\varepsilon = 0.05$ or $\varepsilon = 0.95$; Figure 4.6a and 4.6d, full black line compared to dashed black line). The maximum discrepancies are located in the lower regions (quadrants III/IV), because, in these regions, the thermal boundary layer is significantly thinner when natural convection is considered (e.g. Figure 4.4x). Therefore, the convective and total heat fluxes at the skin are considerably higher.

Regarding the radiative heat flux component at the skin, for $I_g = 0.05$, the discrepancies between considering or neglecting natural convection are below $10\ \%$ (Figure 4.6c and 4.6f, dashed blue line compared to full blue line). For $I_g = 0.25$, it was found that ignoring natural convection can result in over-predictions of up to $27\ \%$ or $38\ \%$ ($\varepsilon = 0.05$ or $\varepsilon = 0.95$) in the upper regions (quadrants I/II), and under-predictions of up to $1.6\ \%$ or $7.8\ \%$ ($\varepsilon = 0.05$ or $\varepsilon = 0.95$) in the lower regions (quadrants III/IV; Figure 4.6c and 4.6f, dashed black line compared to full black line, at $0° < \theta < 180°$ and $180° < \theta < 360°$, respectively). Maximum disagreements are located at $\sim 87°$, which coincides with the position of the thermal plume. These over- and under-predictions of the radiative fluxes at the skin are related to the under- and over-predictions, respectively, of the temperature of the inner fabric, the surface with which the skin exchanges radiant heat. The behaviour of the temperature of the inner fabric, in turn, can be approximated by that of the temperature of the outer fabric, discussed in the following paragraph.

As for the temperature of the outer fabric, for $I_g = 0.05$, disregarding natural convection results in under-predictions of up to $1.4\ \mathrm{K}$ or $1.0\ \mathrm{K}$ ($\varepsilon = 0.05$ or $\varepsilon = 0.95$) in the upper regions (quadrants I/II), and over-predictions of up to $1.3\ \mathrm{K}$ or $1\ \mathrm{K}$ ($\varepsilon = 0.05$ or $\varepsilon = 0.95$) in the lower regions (quadrants III/IV; Figure 4.7, dashed blue line compared to full blue line, at $0° < \theta < 180°$ and $180° < \theta < 360°$, respectively). When $I_g = 0.25$, under-predictions reach $10\ \mathrm{K}$ or $6.3\ \mathrm{K}$ ($\varepsilon = 0.05$ or $\varepsilon = 0.95$) in the upper regions and $2.8\ \mathrm{K}$ or $2.0\ \mathrm{K}$ ($\varepsilon = 0.05$ or $\varepsilon = 0.95$) in the lower regions (Figure 4.7, dashed black line compared to full black line). Maximum discrepancies are again located in the vicinities of $\theta \sim 87°$, the position of the thermal plume (Figure 4.4x).

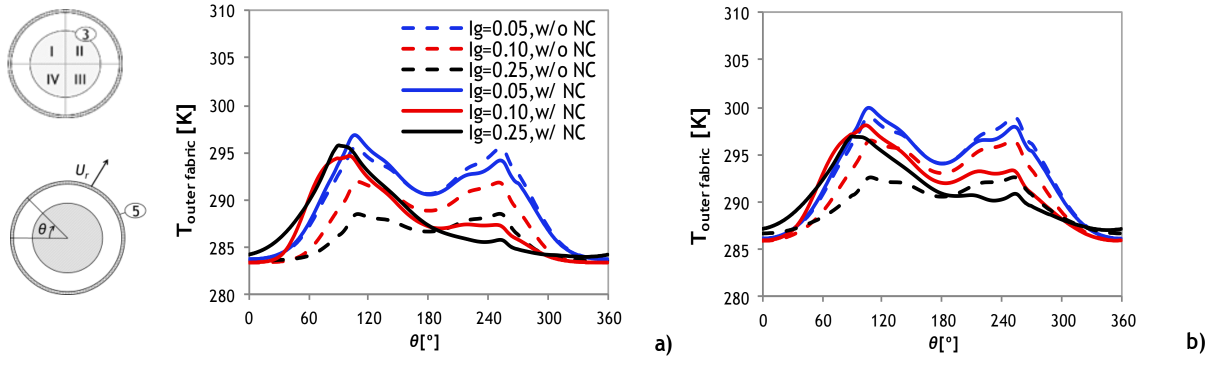

Figure 4.7: Time-averaged temperature around the outer fabric (boundary 5) vs angular position: a) $\varepsilon = 0.05$; b) $\varepsilon = 0.95$. Legend: NC-natural convection.

The intermediate I_g tested (0.10) seems to set off heat transfer by natural convection, since from this value on, the effects of ignoring it are no longer negligible. In fact, the discrepancies in total heat fluxes obtained when neglecting this phenomenon become significant for this value of I_g: over-predictions reach $345\ \%$ or $86\ \%$ $(\varepsilon = 0.05$ or $\varepsilon = 0.95)$ for $0° < \theta < 120°$ and under-predictions are of up to $58\ \%$ or $38\ \%$ $(\varepsilon = 0.05$ or $\varepsilon = 0.95)$ for $120° < \theta < 360°$. Please note that the percentages of over-predictions obtained for $I_g = 0.10$ are only higher than those obtained for $I_g = 0.25$ because the local maxima are higher; on average, discrepancies are higher for the highest I_g. As for radiative heat fluxes, over-predictions reach $33\ \%$ or $37\ \%$ for $0° < \theta < 135°$, and under-predictions $17\ \%$ or $19\ \%$ $(\varepsilon = 0.05$ or $\varepsilon = 0.95)$ for $135° < \theta < 360°$. Temperature of the outer fabric is underestimated by up to $6.7\ \mathrm{K}$ or $4.7\ \mathrm{K}$ $(\varepsilon = 0.05$ or $\varepsilon = 0.95)$ for $0° < \theta < 135°$, and overestimated by up to $4.5\ \mathrm{K}$ or $3.2\ \mathrm{K}$ $(\varepsilon = 0.05$ or $\varepsilon = 0.95)$ for $135° < \theta < 360°$. Therefore, for $Re = 3900$, the threshold over which natural convection can no longer be ignored, is concluded to be $I_g = 0.10$, corresponding to an air gap thickness of $13\ \mathrm{mm}$ when $D_0 = 0.10$ (the actual representative parameter is I_g, not the thickness of the air gap).

Results for time- and space-averaged heat losses at the skin illustrate the discrepancies that are obtained when natural convection is ignored/considered (Figure 4.8, dashed bars compared to full bars). One observes that, for $I_g = 0.05$, the average results are no different (Figure 4.8), again supporting the conclusion that for that value of I_g, natural convection does not play an important role on heat transfer and can therefore be ignored. For $I_g = 0.10$, neglecting natural convection results in a $73\ \%$ underestimation of the average total heat loss for $\varepsilon = 0.05$, while for $\varepsilon = 0.95$ the underestimation is of only $7\ \%$ (Figure 4.8, dashed red bars compared to full red bars). This suggests that for the intermediate I_g (0.10) and for the most relevant value of inner fabric emissivity (0.95), the influence of natural convection can probably be neglected if, for the envisaged application, the focus is only on average heat loss. It should not be neglected, however, if the inner fabric emissivity is low (0.05), or if one is concerned with local heat fluxes. When $I_g = 0.25$, the discrepancies in total heat loss obtained when natural convection is neglected are of $59\ \%$ or $22\ \%$ $(\varepsilon = 0.05$ or $\varepsilon = 0.95)$, again indicating that for higher air gap thicknesses, this phenomenon should not be ignored. Regarding the average radiative heat losses, it is observed that for all values of I_g, there are no significant differences between ignoring or considering natural convection.

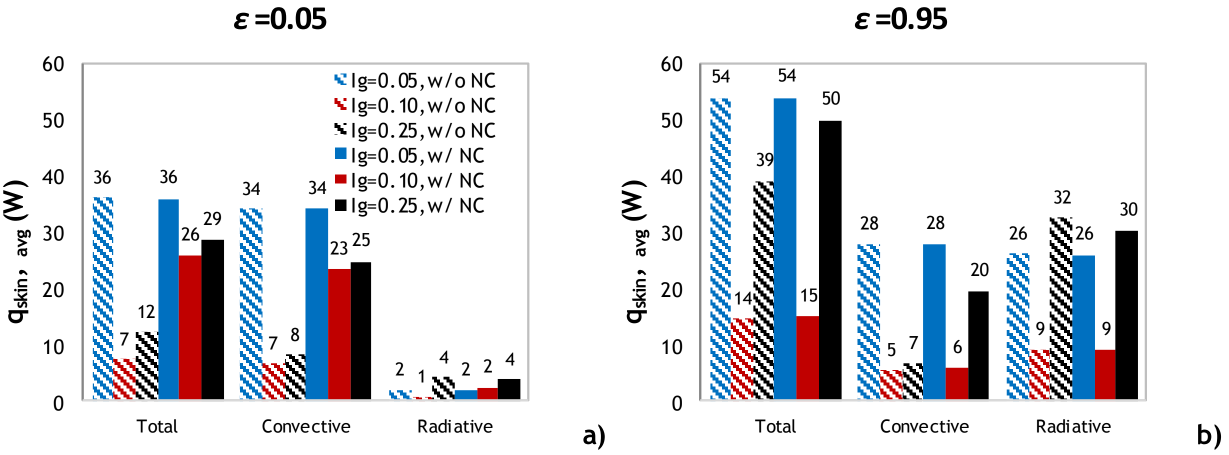

Figure 4.8: Time and space-averaged total, convective and radiative heat loss (in watts) at the skin (boundary 3, Figure 3.1b) as a function of air gap thickness ratio and emissivity, for cases where natural convection is neglected (dashed bars) or considered (full bars). Legend: NC-natural convection.

As a final point, one notices that lowering the emissivity of the inner fabric from $\varepsilon = 0.95$ to $\varepsilon = 0.05$ yield significantly different results both for local and for space-averaged heat loss (Figure 4.6 and 4.8). Radiative fluxes at the skin are reduced, together with the total heat fluxes, indicating that fine-tuning this parameter can help in regulating heat transfer when other parameters cannot be changed or are insufficient to produce the desired results. With this in mind, additional simulations were conducted to analyse the effects of ε, the results of which are discussed in Section 4.3.

4.1.2. Strategy 2: constant diameter of the outer fabric (D_1)

This second subsection is complementary to the preceding one, in that results here presented should allow for conclusions to be drawn regarding the effects of increasing air gap thickness ratio I_g from 0.05 to 0.25 on flow and heat transfer, which were not possible before due to concerns related to the nonconstant inlet air velocity of air not being constant. Two extreme values of I_g were tested (0.05 and 0.25), with $\varepsilon = 0.95$, $Da = 2 \times 10^{-3}$, and considering the effects of natural convection. In this strategy, D_0 was reduced from $0.10\ \mathrm{m}$ to $0.06\ \mathrm{m}$, and D_1 was kept constant at $0.11\ \mathrm{m}$, which means that the characteristic length for flow is constant. Reynolds number is 3900 and the inlet velocity (U_{in}) is constant at $0.54\ \mathrm{m/s}$ (Figure 4.1b). In this case, comparing $I_g = 0.05$ to $I_g = 0.25$ corresponds to, for example, comparing air flow and heat transport around an upper arm with a small air gap thickness ($6\ \mathrm{mm}$) to flow and heat transfer around a lower arm with a high air gap thickness ($28\ \mathrm{mm}$). Note that this strategy is also not ideal, because the diameter of the limb is not kept constant, which means the flow and heat transfer around both limbs may not be exactly the same. This is because the efficiency of heat transfer by convection at the skin, as expressed by the Nusselt number, is a function of the diameter of the limb (Çengel 2002, p.385).

Two simulations were completed, each requiring an average of $57\ \mathrm{h}$ and $2.7\ \mathrm{GB}$ of memory. Mass imbalances were lower than $0.1\ \%$, energy imbalances in the microclimate under $1\ \%$, and energy imbalances at the fabric less than $1\ \%$ for $I_{\mathrm{g}} = 0.05$ and just under $10\ \%$ for $I_{\mathrm{g}} = 0.25$ (see Appendix C). Results for time-averaged radial velocity (dimensionless) and temperature around the outer fabric are in Figure 4.9. Figure 4.10 displays the time-averaged velocity and temperature maps obtained for both cases tested. Figure 4.11 and 4.12 show the results obtained for total, convective and radiative local heat fluxes around the skin (boundary 3, Figure 3.1b) and around the outer fabric (boundary 5, Figure 3.1b), respectively. Results for time- and space-averaged heat losses around the skin and around the outer fabric are in Figure 4.13.

An analysis of Figure 4.9a (black line compared to blue) shows that, near $\theta = 0°/360°$, as well as in the downstream regions, an increase in I_{g} is responsible for higher (absolute) radial velocities of air permeating the fabric. This was expected, but opposite to the results of the previous section, which could be misleading because of the effect of having changed the inlet air velocity (Strategy 1, Figure 4.1a). In the present section, the inlet velocity is kept constant while increasing I_{g} from 0.05 to 0.25 (Strategy 1, Figure 4.1b), making it now possible to draw conclusions regarding the influence of the dimensionless parameter I_{g} on flow and heat transfer around a limb surrounded by a layer of porous fabric.

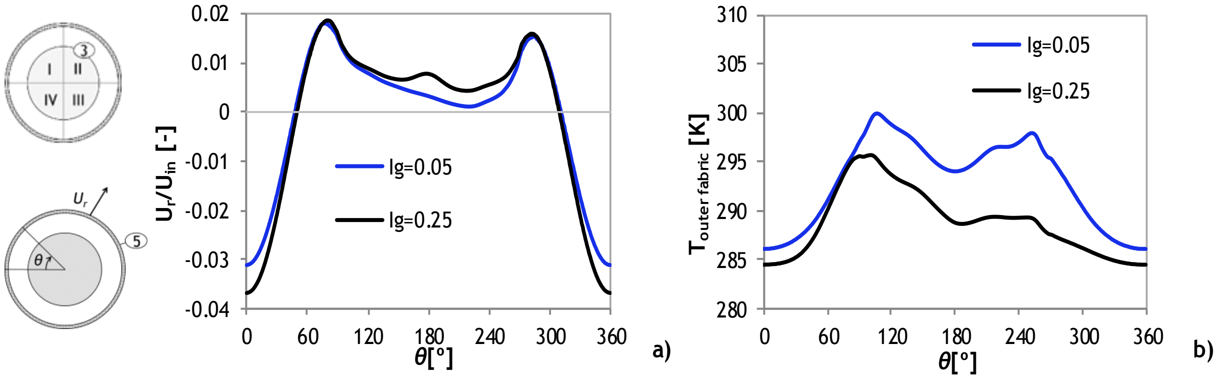

Figure 4.9: Time-averaged radial velocity ratio (a) and temperature (b) around the outer fabric (boundary 5) vs angular position, for two different air gap thickness ratios (0.05 and 0.25) and an inner fabric emissivity of 0.95, considering natural convection. Negative velocities mean that air is entering through the fabric. Legend: NC-natural convection.

Velocity and temperature maps (Figure 4.10) illustrate that an increase in I_{g} from 0.05 to 0.25 causes the symmetrical pattern with respect to $y = 0$, observed at the lowest I_{g} (Figure 4.10a), to disappear and be replaced by an asymmetrical pattern where convection cells can be discerned at either side of the limb (Figure 4.10c). The temperature closer to the fabric is seen to be generally lower for the case with $I_\mathrm{g} = 0.25$ (Figure 4.10d compared to 4.10b), as can also be observed in Figure 4.9b (black line compared to blue line).

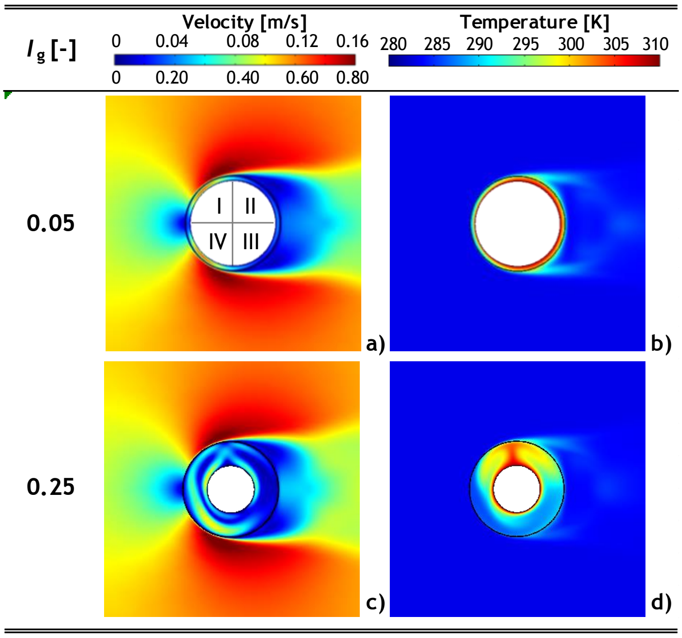

Figure 4.10: Time-averaged velocity magnitude maps (first column) and temperature maps (second column) inside and outside the clothing layer for two different air gap thickness ratios (0.05 and 0.25) and inner fabric emissivity of 0.95, considering natural convection. Colour legends can be found on top of each column; in the velocity legend, the values above it are valid for the regions inside the microclimate, and the ones below are valid outside the microclimate.

The heat fluxes around the skin (boundary 3, Figure 3.1b) are significantly altered when I_g is varied from 0.05 to 0.25 (Figure 4.11). While for $I_\mathrm{g} = 0.05$ the heat fluxes are almost symmetrical between the upper and lower regions (Figure 4.11, blue lines, $0° < \theta < 180°$ and $180° < \theta < 360°$, respectively), for $I_\mathrm{g} = 0.25$ they are asymmetrical (Figure 4.11, black lines). That is because for the higher I_g, the thickness of the air gap is larger, so the characteristic length for natural convection is also larger (increasing the Grashof number), which implies that buoyancy forces become more important. These buoyancy forces are responsible for the asymmetry that is observed in the heat flux as well as the velocity and temperature patterns. They are also responsible for the shift in the position of the heat fluxe local minima and maxima.

Concerning the time-averaged convective heat fluxes at the skin, one observes that increasing I_g causes these fluxes to decrease at $0° < \theta < 100°$ and at $300° < \theta < 360°$ (most of quadrants I/IV), by up to $98\ \%$ (Figure 4.11b). That is because a higher air gap thickness implies a higher distance between the skin and the exterior domain, thus a lower exposure of the local skin to the permeating flow. On the other hand, at $100° < \theta < 300°$ (most of quadrants II/III), convective fluxes at the skin increase with increasing in I_g by up to $190\ \%$, with the highest discrepancy located in quadrant III, near $\theta \sim 240°$. This latter angle corresponds to a local minimum of convective heat flux for $I_g = 0.05$, but to an absolute maximum for $I_g = 0.25$. This is probably because buoyancy forces are much more significant for the higher I_g, increasing the local air velocity near the skin in this region (Figure 4.10c compared to 4.10a, $\theta \sim 240°$) and transporting the warmer air upwards, thereby minimizing the thickness of the thermal boundary layer (Figure 4.10d compared to 4.10b, $\theta \sim 240°$). This non-linear behaviour with increasing I_g again stresses the importance of natural convection when modelling flow and heat transfer in concentric geometries at $Re = 3900$.

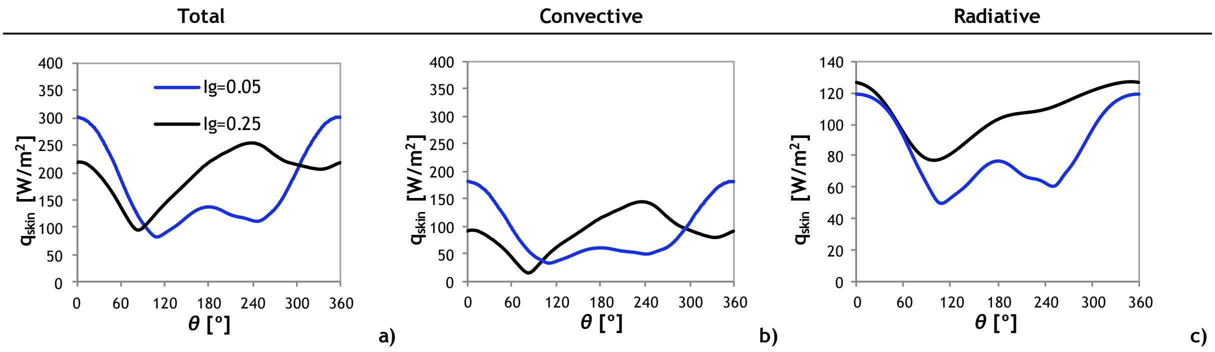

Figure 4.11: Time-averaged total, convective and radiative (a, b and c, respectively) heat fluxes at the skin (boundary 3, Figure 3.1b) vs angular position, evaluated for two different air gap thickness ratios (0.05 and 0.25) and an inner fabric emissivity of 0.95, considering natural convection. Legend: NC-natural convection.

Regarding the radiative heat fluxes, still around the skin, an increase in I_g results in an increase in this heat flux component, particularly in quadrants II, III and IV, where an increase of up to $83\ \%$ is observed (Figure 4.11c, $90° < \theta < 360°$). This is because for the higher I_g (0.25), the inner fabric is at a lower temperature (not very different from that of the outer fabric; Figure 4.9b, $90° < \theta < 360°$). Close to $\theta = 0°/360°$, radiant heat exchange remains practically independent of I_g, the same applying to quadrant I, as in these regions the temperature of the inner fabric does not change significantly with I_g (Figure 4.9b, $0° < \theta < 90°$).

The total heat fluxes at the skin show that increasing the air gap thickness from 0.05 to 0.25 provides protection (i.e. less heat is lost) only in the upstream regions of the skin, while actually causing higher heat losses in the downstream regions (Figure 4.11a). Taking the time- and space-average of the total heat fluxes, one obtains $171\ \mathrm{W/m^2}$ for the case with $I_\mathrm{g} = 0.05$ and $180\ \mathrm{W/m^2}$ for $I_\mathrm{g} = 0.25$, meaning that the higher I_g (higher air gap thickness) is actually less isolating and protective than the lower I_g. Despite being counterintuitive, this behaviour means that for the higher I_g, the distance between the skin and the fabric is sufficiently large to make the increase in convective fluxes (due to increased buoyancy forces) and in radiative fluxes (due to a lower fabric temperature) in some regions counter the decrease in convective fluxes (due to lower exposure to forced convection) in the remaining regions. It seems likely, however, that an intermediate I_g (between 0.05 and 0.25) might result in lower average total heat fluxes than those observed for $I_\mathrm{g} = 0.05$, due to a lower relative importance of heat transfer by natural convection and by radiation.

The results for total, convective and radiative heat fluxes around the fabric (boundary 5, Figure 3.1b) are illustrated in Figure 4.12. A few notes regarding the interpretation of these results are due: the total and convective components should not be regarded as absolute values, since they largely depend on the temperature of the reference enthalpy, here considered $0\ \mathrm{K}$; the radiative heat flux component can be regarded as an absolute value, as it does not depend on the reference state; it then follows that the local relative importance of radiation around the fabric cannot be assessed. Nevertheless, a brief analysis of these results can provide a useful qualitative comparison between cases with $I_\mathrm{g} = 0.05$ and $I_\mathrm{g} = 0.25$, and also lead to a better understanding of how heat transfer occurs at the fabric.

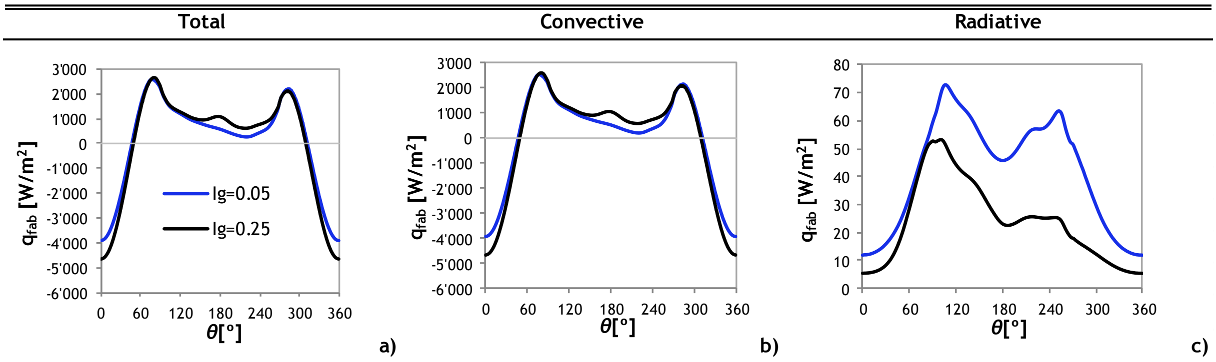

Figure 4.12: Time-averaged total, convective and radiative (a, b and c, respectively) heat fluxes at the fabric (boundary 5, Figure 3.1b) vs angular position, evaluated for two different air gap thickness ratios (0.05 and 0.25) and an inner fabric emissivity of 0.95, considering natural convection. Total and convective heat fluxes were calculated considering $0\ \mathrm{K}$ as the temperature of the reference enthalpy. Negative fluxes mean that heat is entering the microclimate. Legend: NC-natural convection.

The total heat fluxes at the fabric are shown to be overall higher for the case with the higher I_{g}, with the largest differences corresponding to $\theta = 0°/360°$, and to $\theta \sim 180°$ (Figure 4.12a and 4.12b). The variation of the total and convective heat fluxes around θ is closely related with the variation of $U_{\mathrm{r}}/U_{\mathrm{in}}$ as the graphs have the same shape (Figure 4.12a and 4.12b, compared to 4.9a). That is because the local convective flux at the fabric depends on the enthalpy and velocity of the air permeating it. That being so, the higher convective heat fluxes for $I_{\mathrm{g}} = 0.25$ in the aforementioned regions are due to higher radial air velocities (Figure 4.9a), which in turn are caused by higher pressure differences between the inside and outside of the clothing layer. Inversion of the heat flux direction occurs at $47°/312°$ for $I_{\mathrm{g}} = 0.05$, and at $49°/310°$ for $I_{\mathrm{g}} = 0.25$ (Figure 4.12a, intersection with $q_{\mathrm{fab}} = 0$). This could mean that varying I_{g} may have a slight effect on the local direction of heat transfer, since heat transfer reversal occurred approximately $2°$ downstream. These angles should not be confused with the flow reversal angles, which occur at $48°/311°$ for $I_{\mathrm{g}} = 0.05$, and at $50°/309°$ for $I_{\mathrm{g}} = 0.25$.

Radiative fluxes at the fabric are significantly lower for the case with $I_{\mathrm{g}} = 0.25$, especially in the downstream regions (quadrants II/III), where differences amount to up to 65% (Figure 4.12c, $90° < \theta < 270°$). This is because the outer fabric temperature is lower by up to $9\ \mathrm{K}$ in those regions, due to the higher distance between the skin and the fabric. At $\theta \sim 0°/360°$, radiative fluxes and outer fabric temperatures are also lower (Figure 4.12c and 4.9b), by up to $55\ \%$ and $0.6\ \mathrm{K}$, respectively, here probably due to an increased velocity of the cool air permeating the fabric (Figure 4.9a). At $60° < \theta < 90°$ (the location of the thermal plume, Figure 4.10d), increasing I_{g} from 0.05 to 0.25 does not affect heat transfer by radiation (Figure 4.12c), because the temperature of the fabric practically does not vary (Figure 4.9b).

Unfortunately, a thorough comparison of the local heat fluxes at skin and at the fabric was not possible for two reasons: firstly, because the areas of these two surfaces are different, and secondly because the heat fluxes at the fabric include a convective heat flux component (i.e. transport of enthalpy from the air that permeates the fabric), which is a relative value that depends on the temperature of the reference state. This does not, however, undermine a generalist qualitative comparison of these curves. Such a comparison shows that the pattern of heat transport in these two boundaries is quite different, since the local maxima and minima for heat fluxes do not occur at the same angular positions (Figure 4.11 compared to 4.12). This suggests that for certain applications, it might be important to independently analyse heat fluxes both at the fabric and at the skin.

It is observed that radial velocity, outer fabric temperature, and heat fluxes at the skin and at the fabric all widely vary with angular position (Figure 4.9a-b, 4.11 and 4.12), pointing out that a space-averaged approach to heat transfer problems in the present geometry can withhold important information regarding local, and possibly important, variations in temperature and fluxes. For example, for $I_\mathrm{g} = 0.05$, temperature variations around the outer fabric are of up to $14\ \mathrm{K}$ and radiative flux variations reach $143\ \%$. At the skin, convective fluxes varied by up to $66\ \%$, and radiative fluxes by up to $82\ \%$.

Time- and space-averaged convective and radiative heat losses at the skin and at the fabric, weighed against the total heat losses, provide a good notion of the relative importance of these phenomena on heat transfer at the skin and at the fabric (Figure 4.13).

At the skin, convection and radiation have a similar share of the total heat loss, corresponding to $52\ \%$ and $48\ \%$ for $I_\mathrm{g} = 0.05$ and to $44\ \%$ and $56\ \%$ for $I_\mathrm{g} = 0.25$, respectively (Figure 4.13a). These results suggest that, at the skin, convection loses importance and radiation gains importance with increasing I_g. This is consistent with what had been observed on a local level (Figure 4.11b-c) and supports the notion that an increased air gap thickness decreases losses due to convection, but increases those due to radiation. Please note that the total heat loss for $I_\mathrm{g} = 0.25$ is only lower than for $I_\mathrm{g} = 0.05$ because the surface area of skin is also lower, since when using Strategy 2, to increase I_g implied the assumption of a narrower limb (Figure 4.1b). The comparison can only be fair if one looks at the average heat fluxes (in watts per square meter), calculated to be $171\ \mathrm{W/m^2}$ for $I_\mathrm{g} = 0.05$ and $180\ \mathrm{W/m^2}$ for $I_\mathrm{g} = 0.25$, as discussed further above.

At the fabric, convection represents $73\ \%$ of the total heat losses for $I_\mathrm{g} = 0.05$, and $76\ \%$ for $I_\mathrm{g} = 0.25$, indicating that the weight of that heat transfer mechanism does not change with varying I_g (Figure 4.13b). As expected, at the outer fabric boundary, convection is significantly more important than radiation, since this boundary is exposed to the external convective currents.

Finally, the frequency of vortex shedding, evaluated by the Strouhal number, is the same for both values of I_g (Table 4.1), as expected since Re, inlet velocity and outer diameter D_1 are equal. Grashof and Rayleigh numbers increase by two orders of magnitude when I_g is increased from 0.05 to 0.25 (Table 4.1), again reinforcing the conclusion that buoyancy forces become more important with increasing air gap thickness.

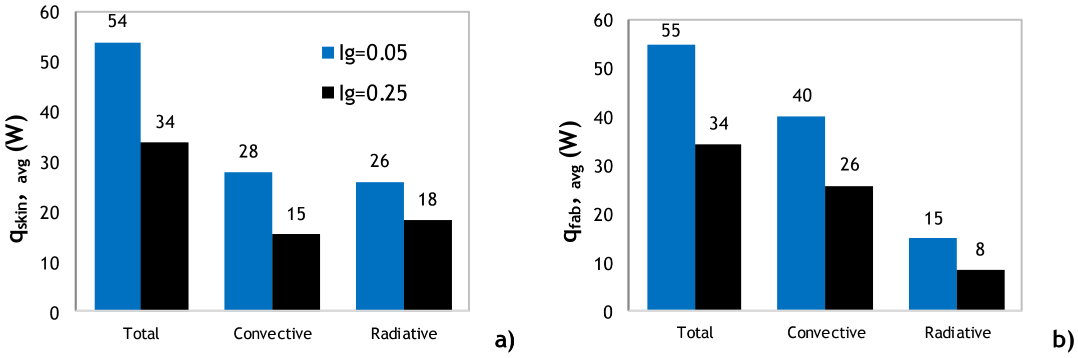

Figure 4.13: Time- and space-averaged total, convective and radiative heat loss (in watts) evaluated for two different air gap thickness ratios (0.05 and 0.25) and an inner fabric emissivity of 0.95, considering natural convection: a) at the skin (boundary 3, Figure 3.1b); b) at the fabric (boundary 5, Figure 3.1b). Legend: NC-natural convection.

Table 4.1: Results for Strouhal, Grashof and Rayleigh numbers, for two values of air gap thickness ratio (0.05 and 0.95), considering natural convection.

l_g [-]	**0.05**	**0.25**
***St* [-]**	0.23	0.23
***Gr* [-]**	3.6 x 10^2	5.7 x 10^4
***Ra* [-]**	2.5 x 10^2	4.1 x 10^4

4.2. Influence of the fabric permeability (Darcy number)

The effects of altering the permeability of the fabric (K) that surrounds the skin were studied by performing numerical simulations for three different Darcy numbers ($Da = K/{H_{\mathrm{fab}}}^2$): 4×10^{-5}, 2×10^{-4} and 2×10^{-3}, values that fall within the range with practical relevance (Sobera 2006). The effect of each Da was studied for simulations where natural convection was either considered or neglected, and for two extreme values of emissivity of the inner fabric ($\varepsilon = 0.05$ and $\varepsilon = 0.95$). Parameter I_{g} was kept constant at 0.20 and so were the other relevant geometrical and physical parameters (please refer to Appendix B for details). Twelve simulations were run, that individually took an average of $42\ \mathrm{h}$ to compute and required up to $3.2\ \mathrm{GB}$ of memory. Mass imbalances for this set of test cases were under $0.1\ \%$, energy imbalances at the microclimate under $0.5\ \%$, and at the fabric these were generally below $10\ \%$, except for cases with lower emissivity, where natural convection was ignored, for which imbalances reached nearly $23\ \%$. A complete table with computational costs and mass and energy imbalances, along with a discussion, can be found in Appendix C.

The above described parametric studies aim at understanding the effects of increasing Da on the flow and heat transfer in the microclimate close to the skin. Two parallel objectives are to find out whether there is a range of Da where ignoring natural convection in such models is acceptable, and to evaluate if changing the emissivity of the inner fabric can significantly alter the flow or heat transfer results.

Velocity and temperature maps (Figure 4.14) provide a useful overview of the results obtained. These allow for some key qualitative conclusions to be drawn, which will be quantified and discussed in more detail further down in this section. Firstly, when natural convection is neglected, an increase in Darcy number leads to higher velocities in the microclimate, especially in the upstream region (quadrants I and IV). As a consequence, temperatures in that region decrease, whereas downstream they increase, with increasing values of Da. This was expected since a higher Da (higher permeability) implies that more air is able to permeate through the fabric (Figure 4.15) and transport heat.

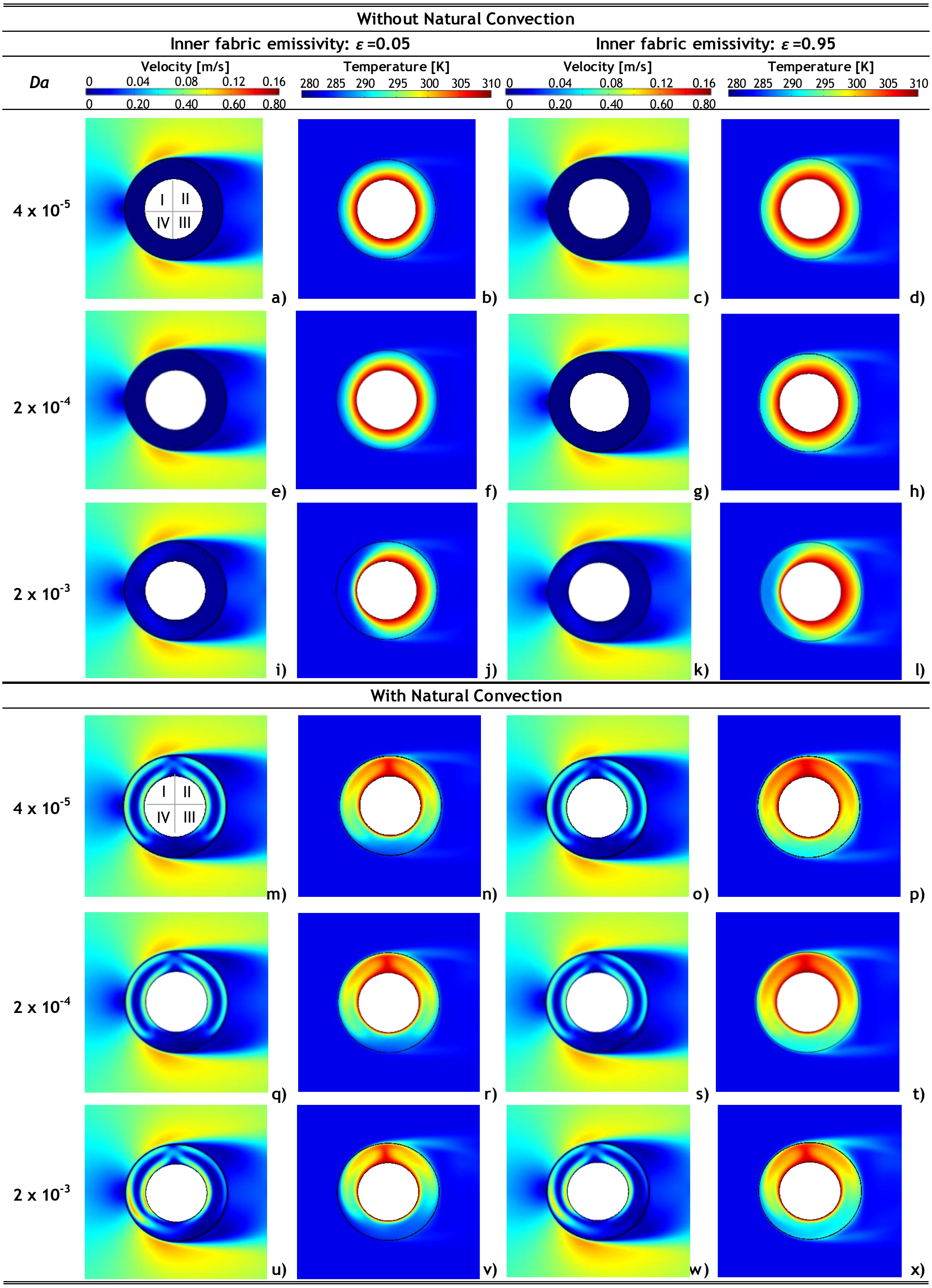

Figure 4.14: Time-averaged velocity magnitude maps (first and third columns) and temperature maps (second and fourth columns) inside and outside the clothing layer for three different Darcy numbers (4×10^{-5}, 2×10^{-4}, 2×10^{-3}) and two emissivities (0.05 and 0.95), for cases where natural convection is either ignored (a-l) or considered (m-x). Colour legends can be found on top of each column; in the velocity legend, the values above it are valid for the regions inside the microclimate, and the ones below are valid outside the microclimate.

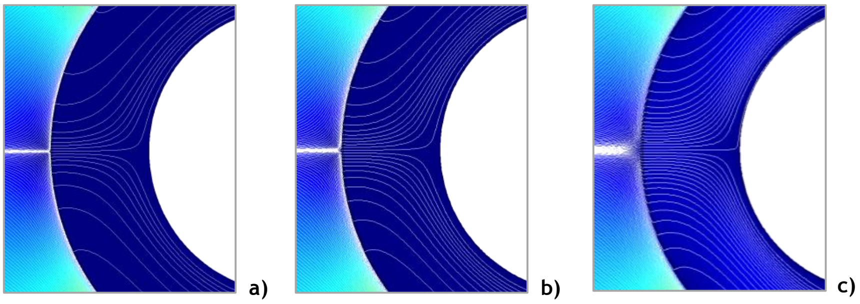

Figure 4.15: Time-averaged velocity magnitude and streamlines at the upstream region of the microclimate, for three different Darcy numbers for $\varepsilon = 0.95$ and neglecting natural convection: a) $Da = 4 \times 10^{-5}$, b) $Da = 2 \times 10^{-4}$ and c) $Da = 2 \times 10^{-3}$.

At the lowest Da (4×10^{-5}), the air permeability of the fabric is close to wind-barrier materials (Gibson 2009, p.5), which is confirmed by the near-zero velocities and the almost axisymmetric temperature pattern in the enclosure (Figure 4.14b,d). Velocities and temperatures in the microclimate are observed to be practically symmetrical with respect to $x = 0$ for that Da, which can be taken to mean that air permeating to the enclosure has practically no effect on the internal flow and heat transfer (e.g. Figure 4.14a,b). The results for the intermediate Da (2×10^{-4}) are almost equal to those of the previous case (Figure 4.14e-h), which seems to indicate that the effort of lowering Da under 2×10^{-4} in order to reduce the heat loss is probably futile. For the highest Da tested (2×10^{-3}), on the contrary, one observes higher velocities within the microclimate (e.g. Figure 4.14k), as well as lower temperatures (e.g. Figure 4.14l), especially at the upstream quadrants, where the pressure difference between the outside and the inside of the system is larger.

When natural convection is ignored (Figure 4.14a-l), the velocity and temperature maps are observed to be symmetrical between the upper and lower regions of the microclimate (quadrants I/II and III/IV, respectively) for all tested Darcy numbers and emissivities. This was anticipated given that, when natural convection is neglected, the buoyancy forces that generate convection currents and make the flow asymmetrical are not included in the model. Raising the inner fabric emissivity from 0.05 to 0.95 has no visible effect on the velocity distribution or magnitude (Figure 4.14a,e,i, compared to 4.14c,g,k), but the temperature in the microclimate is overall higher for the cases with the highest ε (Figure 4.14b,f,j, compared to 4.14d,h,l).

When the effect of natural convection is duly considered, one observes a deep change on the velocity and temperature maps in the microclimate (Figure 4.14m-x): two convection cells are formed, upstream and downstream the limb, that drastically change the velocity and temperature distributions (e.g. Figure 4.14o,p) An asymmetry exists between the upper and lower regions of the enclosure, with higher temperatures observed at the top due to the upwards motion of the warmer (less dense) fluid elements and the downwards motion of the colder (denser) fluid elements. Otherwise, the conclusions drawn concerning the effects of varying the permeability of the fabric remain the same: increasing Da causes the velocities to be higher (e.g. Figure 4.14w compared to 4.14o) and the temperatures to be generally lower (e.g. Figure 4.14x compared to 4.14p) in the microclimate.

The effect of permeability on heat transfer in the microclimate can be assessed by looking at the local time-averaged heat fluxes around the skin (Figure 4.16) and around the outer fabric (Figure 4.17). At the skin, heat fluxes are the most homogeneous for the lowest Da (4×10^{-5}; Figure 4.16, blue lines), which is consistent with the more regular thickness of the thermal boundary layer around it (e.g. Figure 4.14d and 4.14p).

When natural convection is neglected (e.g. Figure 4.16d, dashed lines), total heat fluxes at the skin are symmetrical between the upper ($0° < \theta < 180°$) and lower ($180° < \theta < 360°$) regions of the limb, which agrees with previous observations concerning the symmetry of the velocity and temperature distributions (Figure 4.14a-l). Raising Da from 2×10^{-4} to 2×10^{-3} (i.e. raising air permeability) makes the total heat fluxes at the upstream regions (quadrants I and IV) increase by up to $110\ \%$ or $37\ \%$ ($\varepsilon = 0.05$ or $\varepsilon = 0.95$, respectively), and decrease at the downstream regions (quadrants II and III) by up to $25\ \%$ or 10% ($\varepsilon = 0.05$ or $\varepsilon = 0.95$). This is because increasing Da causes more air to enter the microclimate due to $\sim 950\ \%$ higher velocities observed upstream of the limb (Figure 4.18, dashed lines, $0° < \theta < 50°, 310° < \theta < 360°$), which in turn are responsible for up to $1\ \mathrm{K}$ or $2\ \mathrm{K}$ ($\varepsilon = 0.05$ or $\varepsilon = 0.95$) lower outer fabric temperatures (Figure 4.19, dashed lines, $0° < \theta < 50°, 310° < \theta < 360°$) and for a thinner thermal boundary layer in this region (upstream the limb). Consequently, the driving force for heat transfer by radiation and convection is increased. At the same time, the air that permeates to the microclimate pushes the warmer air in the direction of the flow, making the outer fabric temperature up to $1.5\ \mathrm{K}$ or $1\ \mathrm{K}$ ($\varepsilon = 0.05$ or $\varepsilon = 0.95$) higher at $50° < \theta < 310°$ (Figure 4.19, dashed lines); as a result, the temperature gradient between the skin and inner fabric decreases and the thermal boundary layer thickens with increasing Da, so heat transfer by radiation and by convection reduces (Figure 4.16c,b and 4.24f,e; dashed black line compared to dashed blue line, $50° < \theta < 310°$). As for radiative heat transfer (Figure 4.16c,f, dashed lines), increasing Da causes radiative fluxes to increase by $2\ \%$ or $9\ \%$ ($\varepsilon = 0.05$ or $\varepsilon = 0.95$) at $0° < \theta < 75°$ and $285° < \theta < 360°$, and decrease by $5\ \%$ or $6\ \%$ ($\varepsilon = 0.05$ or $\varepsilon = 0.95$) at $75° < \theta < 285°$.

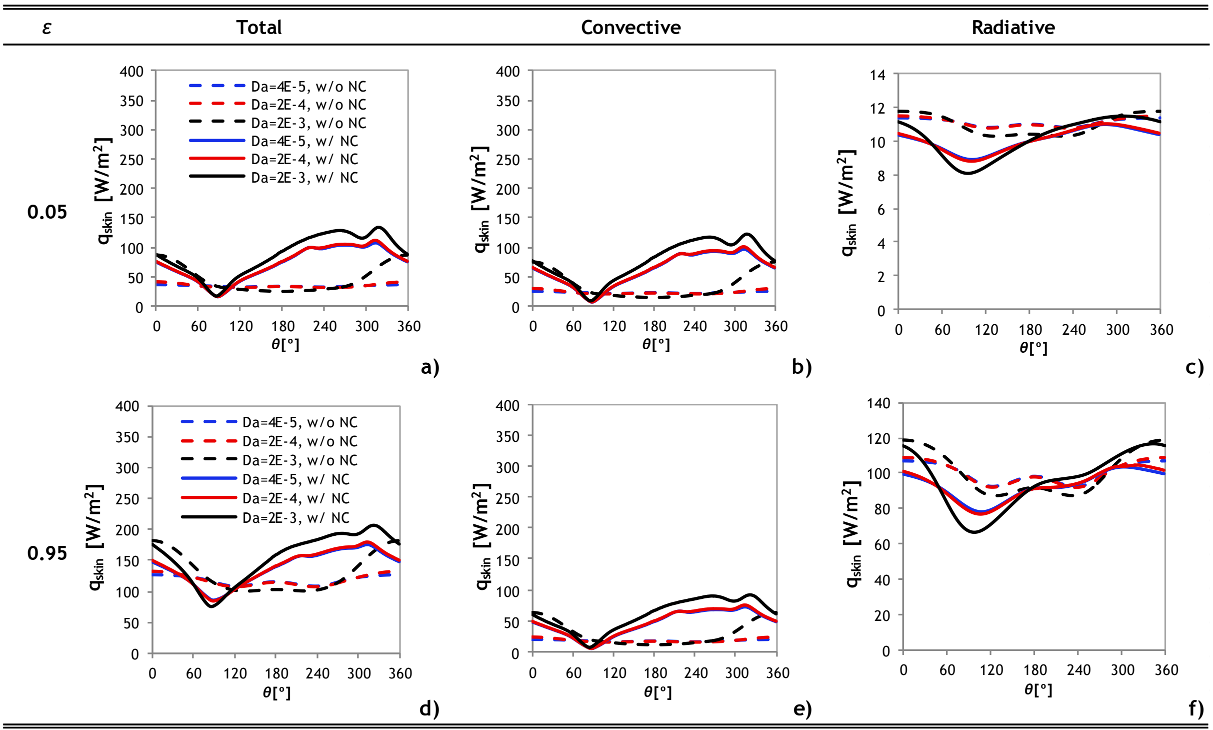

Figure 4.16: Time-averaged total, convective and radiative (a,d; b,e; c,f, respectively) heat fluxes at the skin (boundary 3, Figure 3.1b), evaluated for three different fabric Darcy numbers (4×10^{-5}, 2×10^{-4}, 2×10^{-3}) and two different inner fabric emissivities (0.05 and 0.95), for cases where natural convection is neglected (w/o NC) or considered (w/ NC). Legend: NC-natural convection.

When natural convection is appropriately considered, an asymmetry is observed in the velocity and temperature maps (Figure 4.14m-x), and consequently on the heat flux patterns. Still at the skin, raising the Darcy number from 2×10^{-4} to 2×10^{-3} led to an increase in total heat fluxes of up to 27 % or 21% ($\varepsilon = 0.05$ or $\varepsilon = 0.95$; Figure 4.16a,d, full lines), except at $\theta \sim 86°$, where fluxes are minimum and remain practically constant. This increase in total fluxes probably has to do with the fact that, due to more air being able to permeate the fabric, velocities in the microclimate are higher, in particular close to the skin (e.g. Figure 4.14w, compared to 4.14s), therefore the thermal boundary layer decreases in thickness, again with the exception of $\theta \sim 86°$. This latter region corresponds to the location of the thermal plume, as observed when studying the effect of air gap thickness ratio (Section 4.1).

Increasing Da increases the velocities in the microclimate and is responsible for the accentuation of differences between the upper and lower regions, as more heat is transported upwards and accumulated in the upper region. The temperature of the outer fabric at this location is consequently raised by up to 3.9 K or 3.1 K ($\varepsilon = 0.05$ or $\varepsilon = 0.95$; Figure 4.19, full lines, $50° < \theta < 170°$) when Da increases from 2×10^{-4} to 2×10^{-3}. On the contrary, the temperature of the outer fabric in the lower regions and inflow regions decreases by as much as 2.5 K or 3 K ($\varepsilon = 0.05$ or $\varepsilon = 0.95$; Figure 4.19, full lines, $0° < \theta < 50°$, $170° < \theta < 360°$). Still at the skin, the relationship between radiative flux and temperature of the inner fabric (approximated by the temperature of the outer fabric) is reverse, or in other words, the flux is higher when the fabric temperature is lower, because the temperature differential between skin and fabric is larger. Consequently, increasing Da causes radiative fluxes to become lower by $9\ \%$ or $15\ \%$ ($\varepsilon = 0.05$ or $\varepsilon = 0.95$) at the upper regions, while increasing them by almost $7\ \%$ or $14\ \%$ ($\varepsilon = 0.05$ or $\varepsilon = 0.95$) in the lower regions (Figure 4.16c,f, full lines).

At the fabric (boundary 5, Figure 3.1b), a different behaviour is observed when increasing Da number, as compared to what occurs at the skin (Figure 4.17, compared to Figure 4.16). The reader is reminded that, as in the previous section (4.1.2), the total and convective components of the local heat flux at the fabric (Figure 4.17) should not be regarded as absolute values, but rather as relative values, dependent on the chosen reference enthalpy and temperature (Appendix F). Radiative heat transfer results, on the contrary, do not depend on the reference state. Heat fluxes at the fabric (Figure 4.17, blue lines) are more homogeneous for the lowest Da (4×10^{-5}), as already observed for the fluxes at the skin.

When neglecting natural convection, the heat transfer reversal angles occurs at $44°/317°$ or $35°/325°$ ($\varepsilon = 0.05$ or $\varepsilon = 0.95$) for $Da = 2 \times 10^{-4}$, while at $Da = 2 \times 10^{-3}$ these occurred at $49°/311°$ or $48°/312°$ ($\varepsilon = 0.05$ or $\varepsilon = 0.95$; Figure 4.17a,d), dashed lines, intersection with $q_{\text{fab}} = 0$). This means that increasing Da affects the local direction of heat transfer by making the heat transfer reversal occur approximately $5°$ or $12°$ ($\varepsilon = 0.05$ or $\varepsilon = 0.95$) downstream. Flow reversal occurs at $48°/313°$ for $Da = 2 \times 10^{-4}$, and at $49°/311°$ for $Da = 2 \times 10^{-3}$, regardless of the emissivity ε.

The largest change in total heat fluxes at the fabric when Da is raised from 2×10^{-4} to 2×10^{-3} occurs upstream the clothed limb (close to $\theta = 0°/360°$), and the second largest at $\sim 78°$ and $282°$ (Figure 4.17a,d). These regions correspond to where the velocities of air entering or exiting the microclimate, respectively, are highest (Figure 4.18, dashed lines), thus, they are regions where increasing Da causes the most important changes (up to $912\ \%$ or $850\ \%$ higher velocities, when Da increases from 2×10^{-4} to 2×10^{-3}). In fact, the shape of the total and convective heat fluxes around the fabric is deeply correlated to the radial velocities in this place (Figure 4.18), as expected since convective heat transfer at this boundary is dominant. Interestingly, the local radiative heat transfer at the fabric (Figure 4.17c,f) is also affected by an increase in permeability, due to the changes in the local temperature of the fabric, because of the varying convective heat fluxes (Figure 4.17b,e). Upstream of the clothed limb (quadrants I and IV, $-90° < \theta < 90°$), radiative fluxes decrease by up to $74\ \%$ or 40% ($\varepsilon = 0.05$ or $\varepsilon = 0.95$) when Da varies from 2×10^{-4} to 2×10^{-3}, owing to a decrease in temperatures in this region of $1\ \mathrm{K}$ or $2\ \mathrm{K}$ ($\varepsilon = 0.05$ or $\varepsilon = 0.95$), that reduces the temperature gradient between the fabric and ambient air. At the downstream regions (quadrants II and III, $90° < \theta < 270°$), radiative fluxes increase by up to $59\ \%$ or $16\ \%$, since fabric temperature increases by $1.5\ \mathrm{K}$ or $1.1\ \mathrm{K}$ ($\varepsilon = 0.05$ or $\varepsilon = 0.95$).

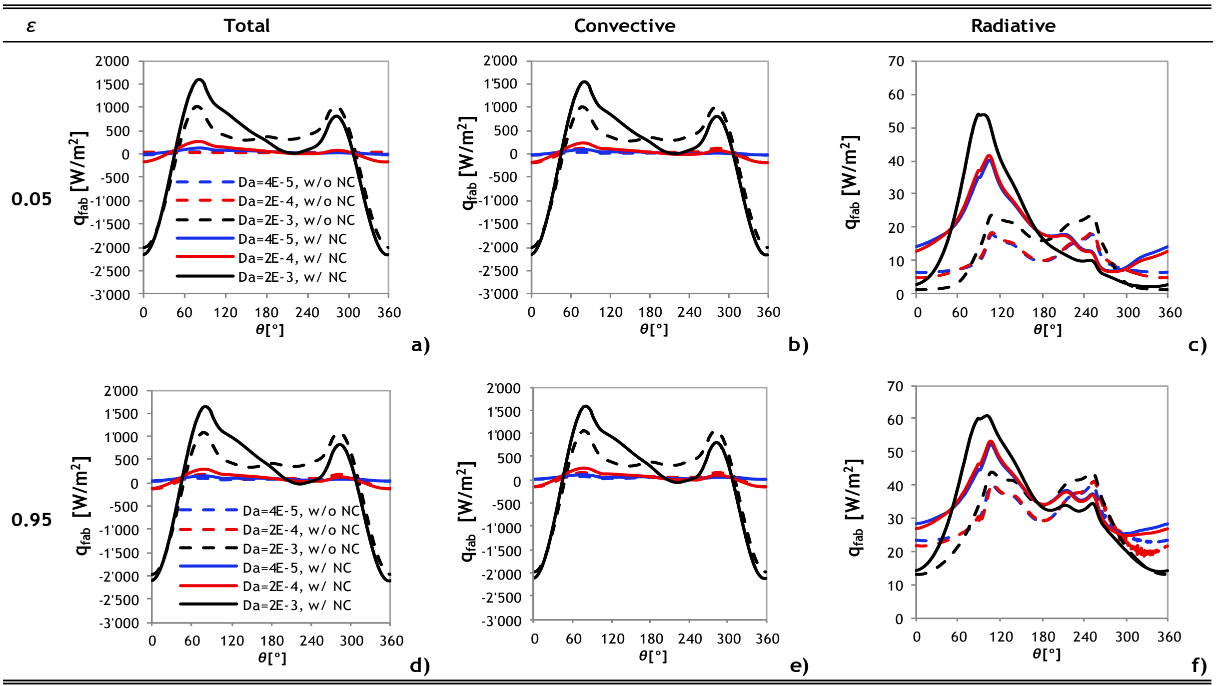

Figure 4.17: Time-averaged total, convective and radiative (a,d; b,e; c,f, respectively) heat fluxes at the fabric (boundary 5, Figure 3.1b), evaluated for three different fabric Darcy numbers (4×10^{-5}, 2×10^{-4}, 2×10^{-3}) and two different inner fabric emissivities (0.05 and 0.95), for cases where natural convection is ignored or considered. Total and convective heat fluxes were calculated considering $\mathbf{0\ K}$ as the temperature of the reference enthalpy. Negative fluxes mean that heat is entering the microclimate. Legend: NC-natural convection.

When natural convection is duly considered (Figure 4.17a,d, full lines), a larger Da implies larger total heat flux magnitudes in quadrants I, II and IV, and smaller in quadrant III, in line with the variations of velocity (Figure 4.18, full lines). Heat transfer reversal occurs at $34°/310°$ or $28°/320°$ ($\varepsilon = 0.05$ or $\varepsilon = 0.95$) for $Da = 2 \times 10^{-4}$, while at $Da = 2 \times 10^{-3}$ these occur at $49°/311°$ or $45°/307°$ ($\varepsilon = 0.05$ or $\varepsilon = 0.95$; Figure 4.17a,d, full lines, intersection with $q_{\mathrm{fab}} = 0$). Flow reversal occurs at $42°/306°$ for $Da = 2 \times 10^{-4}$, and at $47°/308°$ for $Da = 2 \times 10^{-3}$. The behaviour of the total heat flux with increasing Da is similar to what is observed when natural convection is neglected (Figure 4.17a,d, full lines, as compared to dashed lines), the difference being that heat fluxes become asymmetrical between the upper and lower regions of the clothed limb, in agreement with the observed velocity and temperature maps (Figure 4.14m-x). The effect of increasing Da on total heat fluxes at the fabric is most important in quadrant III, as velocities in this region increased by more than $1128\ \%$ or $1241\ \%$ ($\varepsilon = 0.05$ or $\varepsilon = 0.95$). At θ close to $0°$ the effects are also substantial, as velocities increased by $760\ \%$ or $747\ \%$ ($\varepsilon = 0.05$ or $\varepsilon = 0.95$). As for the radiative heat fluxes, the maximum is located at $\theta \sim 89°$ (Figure 4.17c,f, full lines), coinciding with the maximum outer fabric temperature (Figure 4.19). In the same way, radiative fluxes are minimum at $\theta \sim 0°$, because outer fabric temperature is lowest in this region, thus reducing the temperature gradient between the surface and ambient. Increasing Da from 2×10^{-4} to 2×10^{-3} decreases the radiative fluxes by up to $80\ \%$ or $47\ \%$ ($\varepsilon = 0.05$ or $\varepsilon = 0.95$) at $0° < \theta < 50°$ and $170° < \theta < 360°$, and increases them by up to $50\ \%$ or $32\ \%$ ($\varepsilon = 0.05$ or $\varepsilon = 0.95$) at $50° < \theta < 170°$ (Figure 4.17c,f).

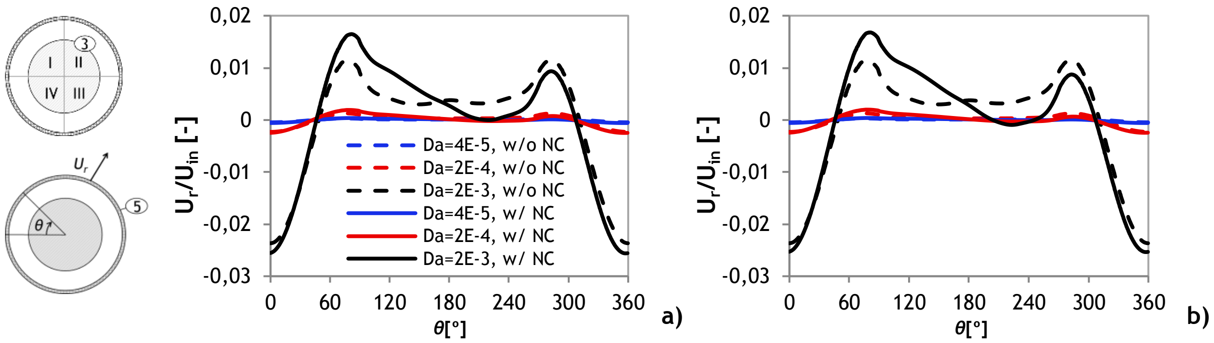

Figure 4.18: Time-averaged radial velocity ratio at the outer fabric (boundary 5) vs angular position: a) $\boldsymbol{\varepsilon = 0.05}$; b) $\boldsymbol{\varepsilon = 0.95}$. Negative velocities mean that air is entering through the fabric. Legend: NC-natural convection.

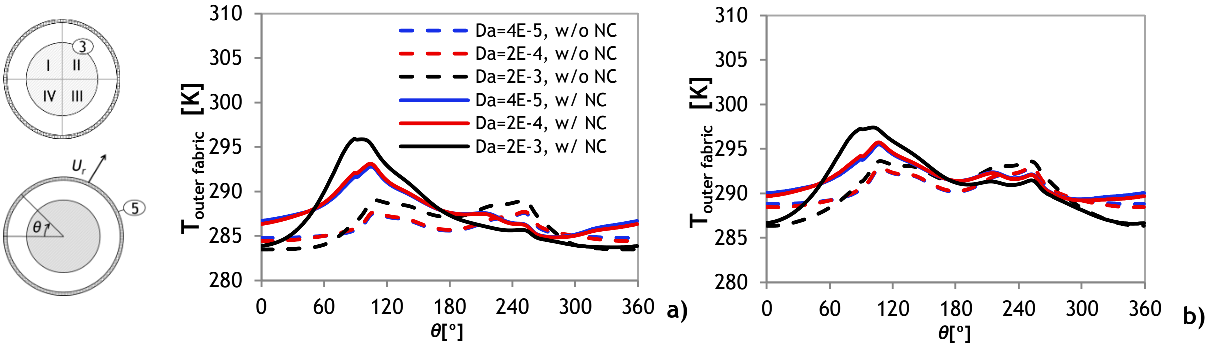

Figure 4.19: Time-averaged temperature around the outer fabric (boundary 5) vs angular position: a) $\boldsymbol{\varepsilon = 0.05}$; b) $\boldsymbol{\varepsilon = 0.95}$. Legend: NC-natural convection.

Another interesting observation when natural convection is duly considered, is that for the highest Da (2×10^{-3}), heat is seen to enter the microclimate at an unexpected region in the third quadrant ($214° < \theta < 231°$ for $\varepsilon = 0.05$, or $191° < \theta < 263°$ for $\varepsilon = 0.95$), as proved by the negative (albeit small) total heat fluxes and radial velocities in this area (Figure 4.17a,d and Figure 4.18, full black line). This and other previous remarks add to the conclusion that natural convection plays an important role on the flow and heat transfer in microclimates near the skin, and should not be ignored in studies of this kind. In fact, failing to model this phenomenon can result both in locally large qualitative errors and in quantitative errors in the prediction of the effects of raising Da. The highest discrepancies corresponded to the highest Darcy number (2×10^{-3}), which, despite counterintuitive, enables the conclusion that for the range tested, natural convection gains importance with increasing Da (e.g. Figure 4.16d, by comparing the discrepancy between the full and dashed black line to that between the full and dashed blue line). At the skin, the mentioned discrepancies at that Da can amount to $100\ \%$ or $55\ \%$ ($\varepsilon = 0.05$ or 0.95) over-predictions at $0° < \theta < 100°$ and $77\ \%$ or $44\ \%$ ($\varepsilon = 0.05$ or 0.95) under-predictions at $100° < \theta < 360$ of the total heat flux (Figure 4.16a,d, full black lines compared to dashed black lines); for radiative fluxes, disagreements are of $34\ \%$ or $42\ \%$ ($\varepsilon = 0.05$ or 0.95) over-predictions at $0° < \theta < 180°$ and $6\ \%$ or $11\ \%$ ($\varepsilon = 0.05$ or 0.95) under-predictions at $180° < \theta < 360°$ (Figure 4.16c,f, full black lines compared to dashed black lines). For the temperature of the outer fabric under-predictions are of $9.4\ \mathrm{K}$ or $6.2\ \mathrm{K}$ ($\varepsilon = 0.05$ or 0.95) at $0° < \theta < 180°$ and over-predictions of $3.3\ \mathrm{K}$ or $2.2\ \mathrm{K}$ ($\varepsilon = 0.05$ or 0.95) at $180° < \theta < 360°$ (Figure 4.18, full black lines compared to dashed black lines).

Time- and space-averaged total and convective heat loss[2] (in watts) at the skin and at the fabric (Figure 4.20 and 4.21, respectively) show that the mean heat loss is increased when Da increases, for both values of emissivity and for cases with and without natural convection. More specifically, when natural convection is considered, increasing Da from 2×10^{-4} to 2×10^{-3} causes a $17\ \%$ or $11\ \%$ ($\varepsilon = 0.05$ or $\varepsilon = 0.95$) increase in heat loss at the skin; at the fabric, the effect is practically the same, with heat loss increasing by $16\ \%$ or $11\ \%$ ($\varepsilon = 0.05$ or $\varepsilon = 0.95$). Average radiative heat transfer is practically independent Da, which means that this parameter affects the total heat loss almost exclusively through altering the heat transferred by convection.

Time- and space-averaged results again prove that, for the experimentally relevant range of Da, natural convection should not be ignored, since that could lead to underestimations of average total heat losses of $48\ \%$ or $18\ \%$ ($\varepsilon = 0.05$ or $\varepsilon = 0.95$) at the skin, and $41\ \%$ or $16\ \%$ ($\varepsilon = 0.05$ or $\varepsilon = 0.95$) at the fabric (percentages calculated for $Da = 2 \times 10^{-3}$). Another remark can be made by observing that neither the local nor the average heat fluxes are visibly altered when Da is increased from 4×10^{-5} to 2×10^{-4}, which, as noted before, is taken to signify that lowering Da under 2×10^{-4} is of no interest for protective clothing

---

[2] Heat loss was calculated by applying a time and space integral over one vortex shedding period around the respective boundary and multiplying the result by the area of integration (see Appendix G for formulae).

applications where the focus is on heat transfer (Figure 4.20 and 4.21, by comparing blue bars to red bars).

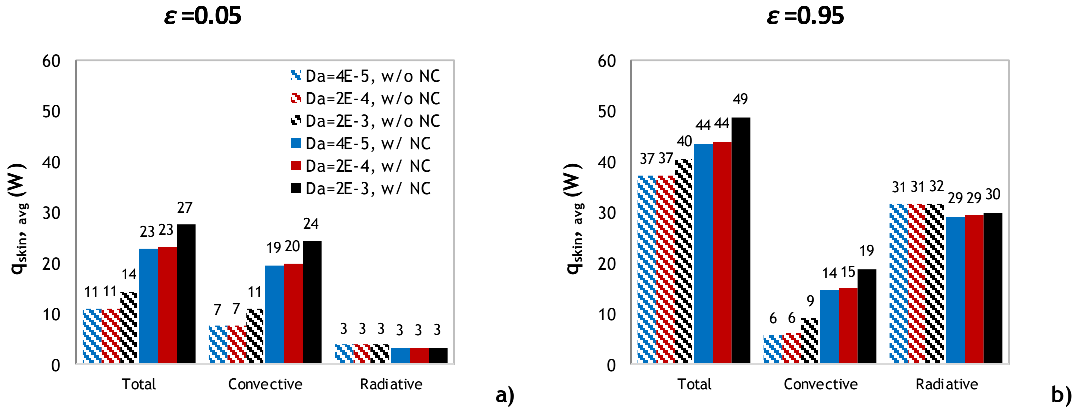

Figure 4.20: Time and space-averaged total, convective and radiative heat loss (in watts) at the skin (boundary 3, Figure 3.1b) as a function of Darcy number and emissivity, for cases where natural convection is neglected (dashed bars) or considered (full bars). Legend: NC-natural convection.

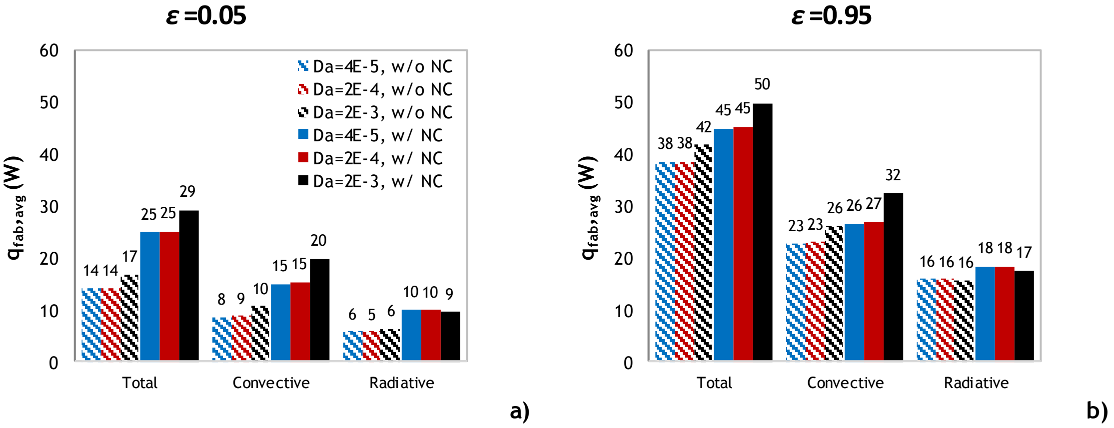

Figure 4.21: Time and space-averaged total, convective and radiative heat loss (in watts) at the fabric (boundary 5, Figure 3.1b) as a function of Darcy number and emissivity, for cases where natural convection is neglected (dashed bars) or considered (full bars). Legend: NC-natural convection.

Furthermore, average total heat transfer at the skin and at the fabric within each test case should be comparable because heat transfer is periodic, i.e. there is no appreciable change in the state of the enclosure from one vortex shedding period to the next (Figure 4.20, compared to 4.21). That is generally true for cases with $\varepsilon = 0.95$, where the differences are bellow $5\ \%$, but not for $\varepsilon = 0.05$, where these reach $27\ \%$ (for $Da = 4 \times 10^{-5}$ and 2×10^{-4}, without natural convection). These discrepancies indicate that a denser mesh would be needed, in particular in situations where the heat loss at the skin is very low (e.g. low emissivity, or low Da), as discussed in more detail in Appendix C.

Lowering the emissivity of the inner fabric causes the radiative and total heat fluxes at the skin to decrease considerably (Figure 4.16), an effect that is analysed in more detail in Section 4.3.

Lastly, Strouhal number is observed to remain constant with increasing Da, which means that the oscillating behaviour of the flow does not change. Grashof and Rayleigh numbers are of the order of 10^4 - 10^5, and increase slightly with the increase of permeability. That is, for the range of Da studied, buoyancy forces seem to become slightly more important when this parameter is increased. This is somewhat counterintuitive, as an increased permeability means that more air enters the microclimate by forced convection, which could be anticipated to make heat transfer by natural convection relatively less important. In reality, what happens is that, for the range of Da studied, velocity in the microclimate increases with increasing Da, in a way that favours heat transfer by natural convection.

Table 4.2: Results for Strouhal, Grashof and Rayleigh numbers, as a function of Darcy number and emissivity, for cases where natural convection is either neglected or considered. Legend: NA-not applicable.

	Without Natural Convection						**With Natural Convection**					
***ε* [-]**	**0.05**			**0.95□**			**0.05**			**0.95□**		
***Da* [-]**	**4×10^{-5}**	**2×10^{-4}**	**2×10^{-3}**	**4×10^{-5}**	**2×10^{-4}**	**2×10^{-3}**	**4×10^{-5}**	**2×10^{-4}**	**2×10^{-3}**	**4×10^{-5}**	**2×10^{-4}**	**2×10^{-3}**
***St* [-]**	0.23	0.23	0.23	0.23	0.23	0.23	0.23	0.23	0.23	0.23	0.23	0.23
***Gr* [-]**	NA	NA	NA	NA	NA	NA	1.1×10^5	1.1×10^5	1.1×10^5	8.5×10^4	8.5×10^4	8.8×10^4
***Ra* [-]**	NA	NA	NA	NA	NA	NA	7.7×10^4	7.7×10^4	7.8×10^4	6.1×10^4	6.1×10^4	6.3×10^4

4.3. Influence of the emissivity of the inner fabric

In this section, the effects of radiation, particularly of the emissivity of the inner fabric ε, are examined. To investigate the effects of decreasing ε on the flow and heat transfer in the microclimate close to the skin, ε was varied from 0.05 to 0.95 (two extremes when it comes to radiative heat transfer) for cases where natural convection is considered, a scenario which was proven in the previous sections to be a more meaningful representation of reality. These extremes correspond to having an inner fabric surface with radiative properties close to a perfect reflector (e.g. fabric with a metallic finish) and close to a blackbody (e.g. common polyester fabrics; Rubežienė et al. 2013, p.410), respectively. The variation was accomplished in increments of 0.30, for an air gap thickness ratio I_{g} of 0.25 (limb diameter $D_0 = 0.1\ \mathrm{m}$). The permeability of the inner fabric, given by the Darcy number, is 2×10^{-3}. Four simulations were completed overall, for which mass imbalances are below $0.1\ \%$, energy imbalances in the microclimate below $1\ \%$, and in the fabric these are generally under $5\ \%$, except for the case with the lowest emissivity, where they reach almost $13\ \%$.

Time-averaged velocity magnitude maps, together with the results for radial velocity ratio around the outer fabric, indicate that decreasing ε from 0.95 to 0.05 has a negligible effect on the flow field (Figure 4.23a compared to 4.23c; Figure 4.22a, blue line compared to grey line). For this reason, the total and convective components of the local heat fluxes around the outer fabric also showed negligible variations with decreasing ε and were therefore excluded from this section. The temperature maps, coupled with the results for the outer fabric temperature, on the other hand, show that decreasing ε from 0.95 to 0.05 significantly decreases the temperatures within the microclimate and at the surface of the clothing (Figure 4.23b compared to 4.23d; Figure 4.22b, blue line compared to grey line), which in turn are responsible for the reduction of the heat fluxes at the skin (Figure 4.24).

Regarding the local heat fluxes around the skin (boundary 3, Figure 3.1b), total fluxes decrease by $23\ \%$ - $75\ \%$ when ε is decreased from 0.95 to 0.05, with maximum differences being found at $\theta \sim 89°$, the location of the thermal plume (Figure 4.24a). This decrease is achieved through a reduction of the radiative fluxes of $86\ \%$ - $89\ \%$ (Figure 4.24c), due to the fact that a low ε (0.05) causes radiation to mostly be reflected by the inner fabric, rather than absorbed. This causes the temperatures in the microclimate to decrease, in particular at the inner fabric, where the decrease amounts to $1\ \mathrm{K}$ - $5\ \mathrm{K}$ (Figure 4.22b, blue line compared to grey line). Unlike the radiative component, convective heat transfer actually increases by $16\ \%$ - $47\ \%$ with decreasing ε (Figure 4.24b, blue line compared to grey line), owing to the temperature decrease in the microclimate and to the lower thickness of the thermal boundary layer (Figure 4.23b compared to 4.23d), which are responsible for a higher driving force for natural convection.

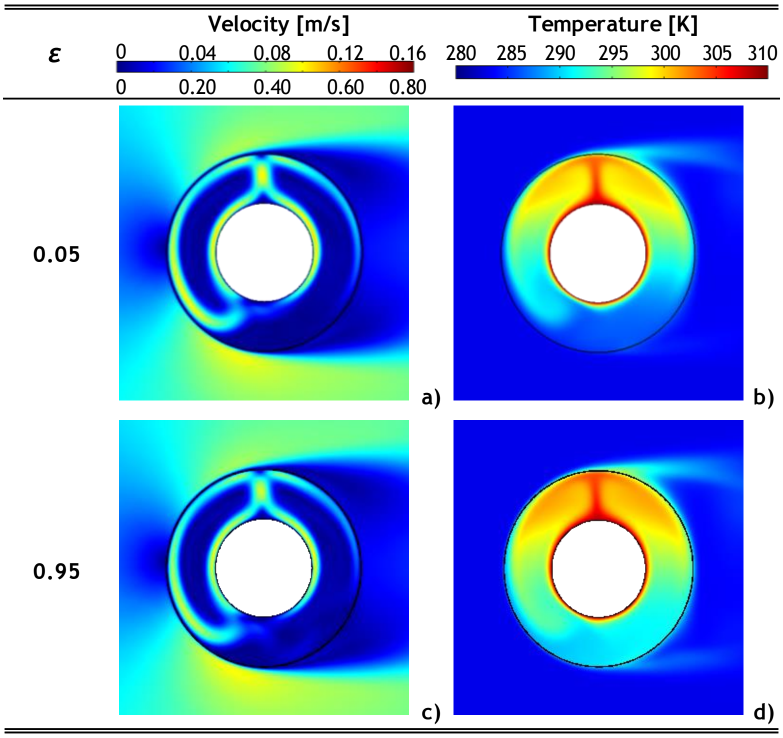

Figure 4.22: Time-averaged velocity magnitude maps (first and third columns) and temperature maps (second and fourth columns) inside and outside the clothing layer for two emissivities (0.05 and 0.95). Colour legends can be found on top of each column; in the velocity legend, the values above it are valid for the regions inside the microclimate, and the ones below are valid outside the microclimate.

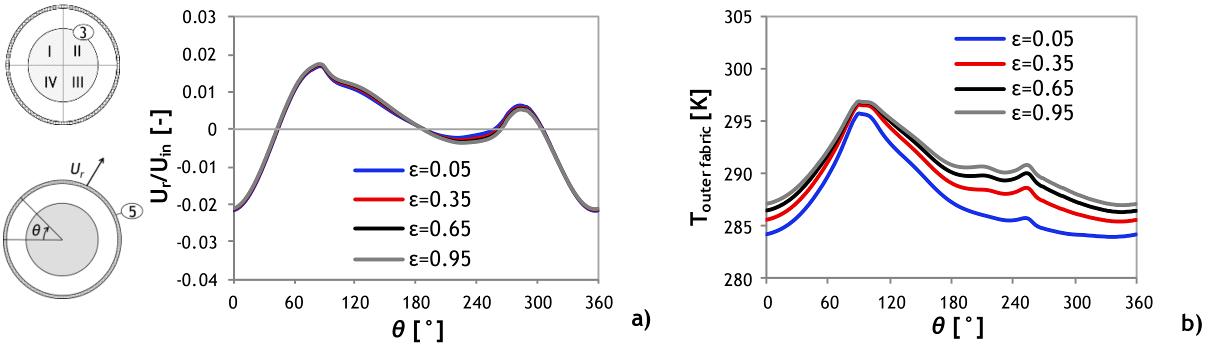

Figure 4.23: Time-averaged radial velocity ratio (a) and temperature (b) at the outer fabric (boundary 5, Figure 3.1b) vs angular position. Negative velocities mean that air is entering through the fabric.

These results suggest that lowering the emissivity of the inner fabric can be an effective way of reducing the heat loss from the microclimate and of altering the relative importance of the heat transfer mechanisms, decreasing that of radiation and increasing that of convection (Figure 4.24). For applications where there are concerns regarding the maximum outer fabric temperatures, observed at $\theta \sim 89°$, lowering ε from 0.95 to 0.05 would result merely in a $1\ \mathrm{K}$

temperature decrease in that area (Figure 4.22b, blue line compared to grey line), rendering this strategy rather ineffective. This is because the existence of natural convection, as discussed extensively in the previous chapters, means that the temperature distributions are asymmetric between the upper and lower regions (quadrants I/II and III/IV, respectively) of the clothed limb, making the temperature decrease most relevant in the lower regions.

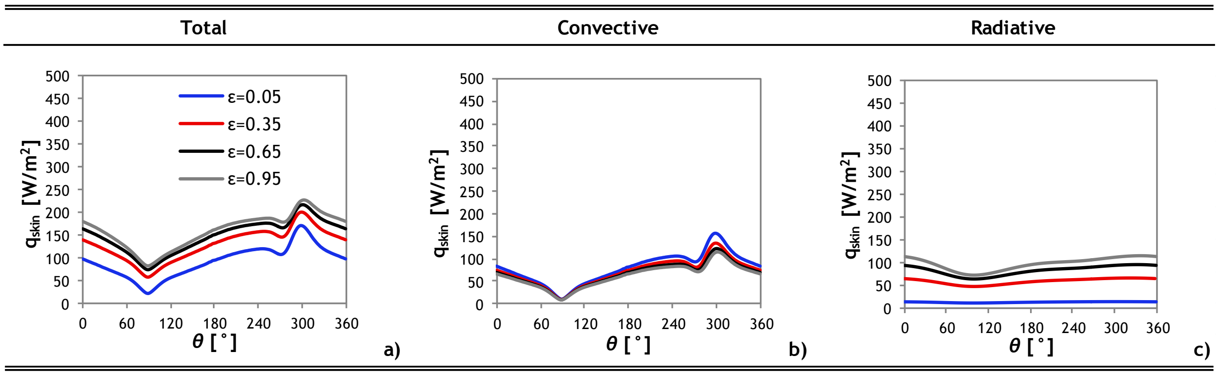

Figure 4.24: Time-averaged total, convective and radiative (a, b and c, respectively) heat fluxes at the skin (boundary 3, Figure 3.1b), as a function of angular position and emissivity.

Total and convective heat fluxes at the skin for $\varepsilon = 0.65$ and for $\varepsilon = 0.95$ are within 10 % of each other (Figure 4.24a,b, black lines compared to grey lines), showing that there is practically no difference in heat transfer when ε is lowered from 0.95 to 0.65. Between $\varepsilon = 0.35$ and $\varepsilon = 0.95$ the differences become appreciable, reaching up to 31 % or 25 % for the total and convective local heat fluxes, respectively (Figure 4.24a,b, red lines compared to grey lines). This indicates that the effort of lowering the emissivity of the inner fabric is only worthwhile if it is reduced to 0.35 or below.

Time- and space-averaged heat loss results at the skin confirm that decreasing ε from 0.95 to 0.05 leads to lower total heat losses at the skin (42 %), due to a decrease in average losses due to radiation (87 %; Figure 4.25, blue bars compared to grey bars). Heat losses due to convection are reduced by 20 %. For $\varepsilon = 0.95$, convective and radiative components share a respective weight of 40 % and 60 %, while for $\varepsilon = 0.05$ the weight is 86 % and 14 %. Average total and convective heat losses for $\varepsilon = 0.65$ again suggest that lowering the emissivity of the inner fabric from 0.95 to 0.65 is rather inconsequential, since the differences between the results for these two values are lower than 10 % (Figure 4.25, black bars compared to grey bars). Therefore, it is once more concluded that only lowering emissivity to below 0.35 is effective in lowering the total heat losses and in altering the relative weight of the mechanisms of heat transfer.

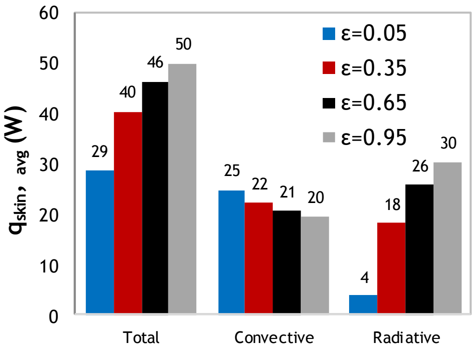

Figure 4.25: Time and space-averaged total, convective and radiative heat loss (in watts) at the skin (boundary 3, Figure 3.1b) as a function of emissivity.

Changing the emissivity of the fabric has no impact on the Strouhal number (Table 4.3). Grashof and Rayleigh numbers, on the other hand, decrease by 23 % when ε decreases from 0.95 to 0.05, supporting the previous conclusion that a decrease in inner fabric emissivity increases the importance of buoyancy forces (i.e. natural convection) due to lower temperatures in the microclimate.

Table 4.3: Results for Strouhal, Grashof and Rayleigh numbers, as a function of emissivity.

ε [-]	**0.05**	**0.35**	**0.65**	**0.95**
***St* [-]**	0.23	0.23	0.23	0.23
***Gr* [-]**	3.7 x 10^5	3.3 x 10^5	3.1 x 10^5	3.0 x 10^5
***Ra* [-]**	2.6 x 10^5	2.4 x 10^5	2.2 x 10^5	2.1 x 10^5

5. Conclusions

This project was set out to provide a deeper understanding of the transport phenomena in microclimates between the human body and a layer of air-permeable clothing, and also how these phenomena are affected by different geometrical parameters or physical properties of the clothing. Numerical models that adequately describe how flow and heat transfer occur in the vicinities of the skin can provide vital information for a wide range of conditions, within a relatively low amount of time. The knowledge of the effects of various parameters can also provide useful information for the development of textiles and protective clothing (e.g. Chemical, Biological, Radiological and Nuclear protective clothing, sportswear).

In this thesis, flow and heat transfer were studied in two dimensions for horizontal, cylindrical microclimates. Reynolds number was kept constant at $Re = 3900$, falling within the very low range of external air velocities ($\sim 0.5\ \mathrm{m/s}$). While this representation is still far from that a moving human body exposed to outdoor air, it provided valuable insight into the influence of the three following parameters: air gap thickness ratio (I_g), fabric permeability (expressed by Darcy number, Da), and emissivity of the inner fabric (ε), with considerably lower computational costs than transient 3D simulations. All three parameters are shown to considerably impact the flow and heat transfer in the microclimate, particularly the former.

First and foremost, increasing I_g was shown to increase the relative importance of natural convection, which led to the development of two counter-rotating convection cells, one at each side of the limb. This motion of the fluid elements creates an asymmetry in the heat flux and temperature distributions in the microclimate, where the upper regions are $\sim 8\ \mathrm{K}$ warmer than the lower regions. These observations highlight the significance of the parameter I_g and of the mechanism of natural convection. They also emphasise the shortcomings of space-averaged approaches to these problems, for which such local variations are ignored.

Secondly, an increment in Da was observed to induce an overall increase of the local heat fluxes around the skin, particularly at $\theta = 0°$ and $180° < \theta < 360°$. It also heightens the asymmetry between the upper and lower regions, leading to the conclusion that, rather counterintuitively, natural convection becomes increasingly important with increasing Da. Moreover, lowering Da below 2×10^{-4} was shown to have no effect on heat transfer when $Re = 3900$.

Thirdly, decreasing ε was proved to be an effective way of decreasing total heat fluxes at the skin. This is accomplished mostly by a decrease in radiative fluxes, while convective fluxes increase slightly. This effect is only interesting, however, if ε is decreased to 0.35 or lower.

Previous research in this topic had recognized the importance of phenomena such as radiation and natural convection in flat and folded clothing microclimates (Couto & Mayor 2013; Oliveira 2015a). The influence of air gap thickness, as well as other parameters such as inlet air velocity and inclination (relative to gravity) had also been reported for flat geometries. In the present study, the relevance of the mentioned heat transfer phenomena and parameter air gap thickness has been confirmed and analysed in detail for cylindrical microclimates at $Re = 3900$. The effects of varying the permeability of the fabric have also been introduced and discussed. To the extent of our knowledge, a comprehensive analysis of heat transfer in cylindrical microclimates which covers radiation, natural convection and flow in porous media has been lacking in literature.

The author recommends further studies in this same geometry, namely of the effects of increasing the inlet air velocity (increasing Re), so as to determine the range of validity of the present conclusions. A three-dimensional representation of the cylindrical microclimate may also be used in order to study the effects of inclination relative to gravity. As a final point, the addition of latent heat and mass transfer models is needed in order to account for the effects of sweating or the presence of potentially harsh chemicals.

6. References

Akiyama, M. & Chong, Q.P., 1997. Numerical analysis of natural convection with surface radiation in a square enclosure. *Numerical Heat Transfer, Part A: Applications*, 32(4), pp.419–433.

Ambesi, D., Kleijn, C.R. & Brasser, P., 2014. Forced convection mass deposition and heat transfer onto a cylinder sheathed by protective garments. *AIChE Journal*, 60(1), pp.353-361.

Ampofo, F. & Karayiannis, T.G., 2003. Experimental benchmark data for turbulent natural convection in an air filled square cavity. *International Journal of Heat and Mass Transfer*, 46, pp.3551–3572.

Andrade, J. et al., 1999. Inertial Effects on Fluid Flow through Disordered Porous Media. *Physical Review Letters*, 82(26), pp.5249–5252.

Angelova, R. a. et al., 2013. Computational modeling and experimental validation of the air permeability of woven structures on the basis of simulation of jet systems. *Textile Research Journal*, 83(18), pp.1887–1895.

Barry, B.J.J. & Hill, R.W., 2003. Computational Modeling of Protective Clothing. *International Nonwovens Journal*, 12(3), pp.25–34.

Bhattacharyya, S. & Singh, A.K., 2011. Reduction in drag and vortex shedding frequency through porous sheath around a circular cylinder. *International Journal for Numerical Methods in Fluids*, 65(6), pp.683–698.

Breuer, M., 2000. A challenging test case for large eddy simulation: high Reynolds number circular cylinder flow. *International Journal of Heat and Fluid Flow*, 21, pp.648–654.

Breuer, M., 1998. Large Eddy Simulation of the Subcritical Flow Past a Circular Cylinder : Numerical and Modeling Aspects. *International Journal for Numerical Methods in Fluids*, 28(9), pp.1281–1302.

Çengel, Y.A., 2002. *Heat Transfer:A Practical Approach* 2nd ed., Mcgraw-Hill.

COMSOL, 2015. CFD Module User's Guide: Version 5.1.

Corcione, M., 2003. Effects of the thermal boundary conditions at the sidewalls upon natural convection in rectangular enclosures heated from below and cooled from above. *International Journal of Thermal Sciences*, 42(2), pp.199–208.

Coulson, J.M. & Richardson, J.F., 1999. Volume 1 - Fluid Flow, Heat Transfer and Mass Transfer. In *Chemical Engineering*. Butterworth Heinemann.

Couto, S. & Mayor, T.S., 2013. *Heat transfer through air-fabric layers with flat and folded surface*, CENTI - Centre for Nanotechnology and Smart Materials, V. N. Famalicão.

Davis, G.D.W., 1983. Natural convection of air in a square cavity - a bench mark numerical solution. *International Journal for Numerical Methods in Fluids*, 3, pp.249–264.

Dhinakaran, S. & Ponmozhi, J., 2011. Heat transfer from a permeable square cylinder to a flowing fluid. *Energy Conversion and Management*, 52(5), pp.2170–2182.

Döbrich, O., Gereke, T. & Cherif, C., 2014. Modelling of textile composite reinforcements on the micro-scale. *Autex Research Journal*, 1(14), pp.10–15.

Dunn, M.W., 2000. *Investigating fluid flow through fabrics*, Philadelphia.

Fourt, L.E. & Hollies, N.R.S., 1970. *Clothing; Comfort and Function*, Marcel Dekker %@

x5327131.

Gibson, P., 2009. Modeling Heat and Mass Transfer from Fabric-Covered Cylinders. *Journal of Engineered Fibers and Fabrics*, 4(1), pp.1–8.

Gozmen, B. et al., 2013. Flow control behind a circular cylinder via a porous cylinder in deep water. *EPJ Web of Conferences*, 01035.

Gozmen, B. & Akilli, H., 2014. Flow control downstream of a circular cylinder by a permeable cylinder in deep water. *Wind and Structures*, 19(4), pp.389–404.

Incropera, F.P. et al., 2007. *Fundamentals of heat and mass transfer* 6th ed., Danvers: John Wiley & Sons.

International Fibre Centre, 2004. Table of fibre densities. Available at: http://www.ifc.net.au/edit/library_fin_dye_finishing/4.1.04 Table of Fibre Densities.pdf? [Accessed May 1, 2015].

Khezzar, L., Siginer, D. & Vinogradov, I., 2012. Natural convection in inclined two dimensional rectangular cavities. *Heat and Mass Transfer*, 48, pp.227–239.

Leithead, C.S. & Lind, A.R., 1964. *Heat Stress and Heat Disorders.*, London: Cassell & CO Ltd.

Min, K. et al., 2007. Heat and moisture transfer from skin to environment through fabrics: A mathematical model. *International Journal of Heat and Mass Transfer*, 50(25-26), pp.5292–5304.

Molla, M.M. et al., 2011. Radiation effects on natural convection laminar flow from a horizontal circular cylinder. *Desalination and Water Treatment*, 30(1-3), pp.89–97.

Murakami, S., Kato, S. & Zeng, J., 2000. Combined simulation of airflow, radiation and moisture transport for heat release from a human body. *Building and Environment*, 35, pp.489–500.

Norberg, C., 1987. *Effects of Reynolds number and a low-intensity freestream turbulence on the flow around a circular cylinder*. Chalmers University of Technology.

Oliveira, D., 2015a. *Numerical simulation of heat transfer around a clothed human limb*, St. Gallen, Switzerland.

Oliveira, D., 2015b. *Numerical simulation on the transport phenomena in microclimates near the skin*. Porto University.

Ozkan, G.M. et al., 2012. Flow around a cylinder surrounded by a permeable cylinder in shallow water. *Experiments in Fluids*, 53(6), pp.1751–1763.

Ozkan, G.M., Akilli, H. & Sahin, B., 2013. Effect of High Porosity Screen on the Near Wake of a Circular Cylinder. *EPJ Web of Conferences*, 01071, pp.1–5.

Psikuta, A. et al., 2012. Quantitative evaluation of air gap thickness and contact area between body and garment. *Textile Research Journal*, 82, pp.1405–1413.

Rief, S. et al., 2011. Modeling and CFD-simulation of woven textiles to determine permeability and retention properties. *AUTEX Research Journal*, 11(3), pp.78–83.

Rossi, R., 2005. Interactions between protection and thermal comfort. In R. A. Scott, ed. *Textiles for protection*. Cambridge: Woodhead Publishing Limited, p. 233.

Rubežienė, V. et al., 2013. Reduction of Thermal Signature Using Fabrics with Conductive Additives. , 19(4), pp.8–10.

Schäfer, M., 2006. *Computational Engineering - Introduction to Numerical Methods*, Berlin: Springer Science & Business Media.

Schäfer, M. & Turek, S., 1996. Benchmark Computations of Laminar Flow Around a Cylinder. In E. H. Hirschel, ed. *Volume 52 of Notes on Numerical Fluid Mechanics*. Vieweg, pp. 547–566.

Shi, J.M. et al., 2004. Heating effect on steady and unsteady horizontal laminar flow of air past a circular cylinder. *Physics of Fluids*, 16(12), p.4331.

Sobera, 2006. *Flow, heat and mass transfer through protective textiles*. Technische Universiteit Delft.

Sobera, M. et al., 2004. A Multi-scale Numerical Study of the Flow, Heat, and Mass Transfer in Protective Clothing. *LNCS*, 3039, pp.637–644.

Sobera, M.P. et al., 2003. Convective heat and mass transfer to a cylinder sheathed by a porous layer. *AIChE Journal*, 49(12), pp.3018–3028.

Sobera, M.P. & Kleijn, C.R., 2008. T-RANS Simulations of Subcritical Flow with Heat Transfer Past a Circular Cylinder Surrounded by a Thin Porous Layer. *Flow, Turbulence and Combustion*, 80(4), pp.531–546.

Soong, C.Y. et al., 1996. Numerical study on mode-transition of natural convection in differentially heated inclined enclosures. *International Journal of Heat and Mass Transfer*, 39(14), pp.2869–2882.

Stringer, R.M., Zang, J. & Hillis, a. J., 2014. Unsteady RANS computations of flow around a circular cylinder for a wide range of Reynolds numbers. *Ocean Engineering*, 87, pp.1–9.

Tremblay, F., 2001. *Direct and large-eddy simulation of flow around a circular cylinder at subcritical Reynolds numbers*. Technische Universität München.

Vivek, V., Sharma, A.K. & Balaji, C., 2012. Interaction effects between laminar natural convection and surface radiation in tilted square and shallow enclosures. *International Journal of Thermal Sciences*, 60, pp.70–84.

White, F., 2011. *Fluid Mechanics* 7th ed., New York: McGraw-Hill.

Appendix A Meshes

Representations of the meshes used for validation of the computational methods can be found in Figure A.1. Meshes 2 and 3 were used solely for validation purposes, as mesh 1 was selected for the parametric studies, according to the procedure detailed in Appendix D.

Meshes were hybrid, with a structured portion on the right-hand side which corresponds to the area where the Kárman vortex street occurs. The remaining areas were unstructured, and local refinement was applied in the microclimate/fabric and immediate vicinities, especially on the downstream side, where vortex shedding occurs. This particular arrangement was chosen so as to minimize the number of elements in the regions further away from the clothed limb and reduce computational cost.

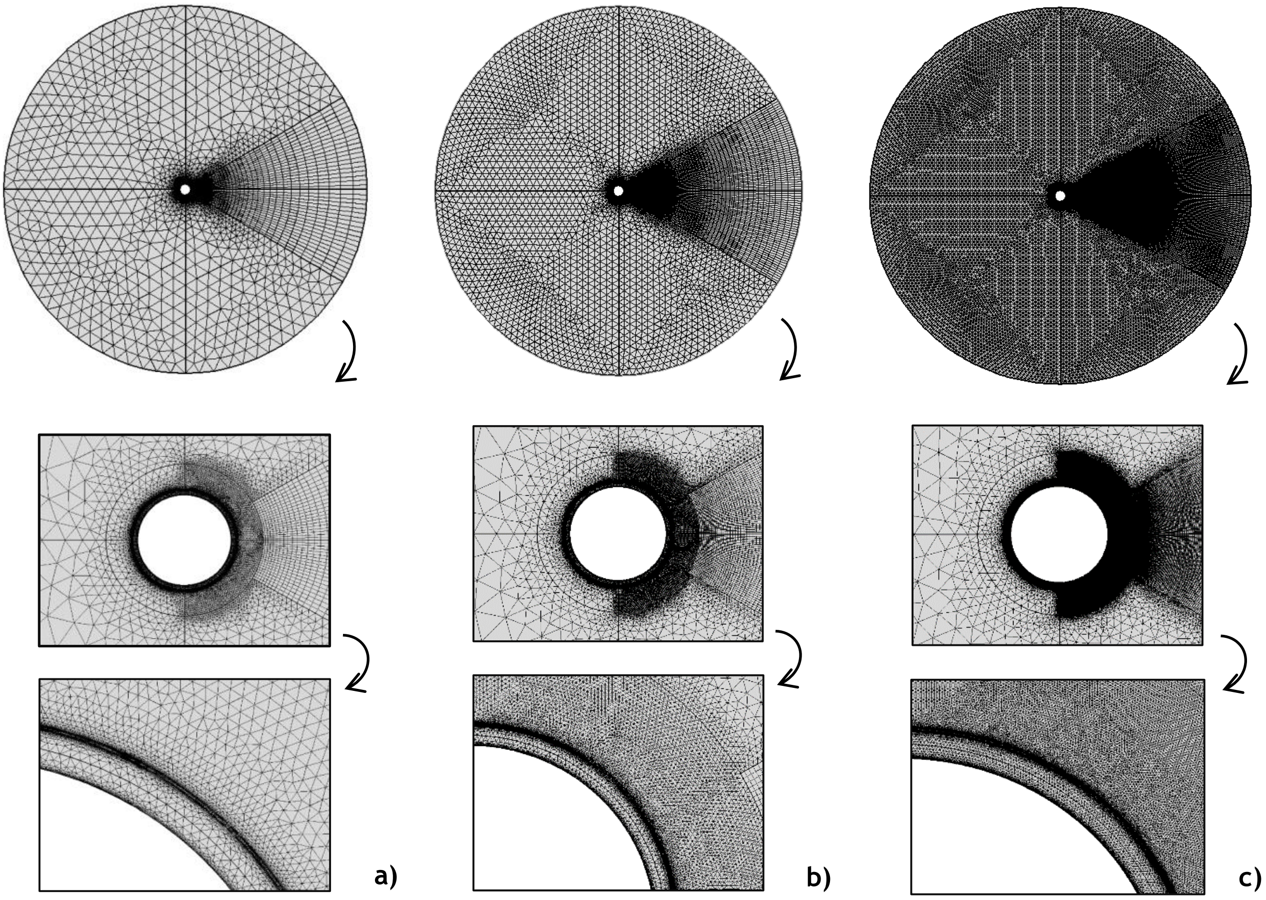

Figure A.1: Representation of meshes used in this study, including zoom-ins of the microclimate area: a) Mesh 1 (38'038 elements); b) Mesh 2 (87'836 elements); c) Mesh 3 (230’664 elements).

Appendix B Overview of simulation cases

Results discussed throughout this thesis were obtained by completing a set of twenty-seven different simulations in COMSOL Multiphysics, where a number of parameters were varied. A comprehensive list of the most relevant physical and geometrical parameters for each test case can be found in Table B.1, along with the respective systematic label.

Table B.1: Parameters used in each simulation case (continued on the next page). Legend: NC-Natural Convection. *Reused cases from a different section.

		Label	ε [-]	NC enabled	l_g [-]	*Da* [-]	*Re* [-]	U_{in} [m/s]	*K* [m^2]	Air permeability [L/min/m]	γ [-]	R_{ct}	k_s [W/K/m]	k_{fab} [W/K/m]	l_c [-]	H_{gap} [m]	H_{fab} [m]	D_0 [m]	D_1 [m]	k_f [W/K/m]
Air gap thickness ratio (l_g)	St. I	lg_0.05_E_0.05_NC_yes_Da_2E-3	0.05	Yes	0.05	2E-03	3900	0.54	6.32E-10	7.19E+04	0.7	0.01	0.11	5.03E-02	5.00E-03	0.0056	5.62E-04	0.10	0.11	0.026
		lg_0.05_E_0.95_NC_yes_Da_2E-3	0.95	Yes	0.05	2E-03	3900	0.54	6.32E-10	7.19E+04	0.7	0.01	0.11	5.03E-02	5.00E-03	0.0056	5.62E-04	0.10	0.11	0.026
		lg_0.10_E_0.05_NC_yes_Da_2E-3	0.05	Yes	0.10	2E-03	3900	0.48	6.32E-10	7.19E+04	0.7	0.01	0.09	4.47E-02	4.45E-03	0.0126	5.62E-04	0.10	0.13	0.026
		lg_0.10_E_0.95_NC_yes_Da_2E-3	0.95	Yes	0.10	2E-03	3900	0.48	6.32E-10	7.19E+04	0.7	0.01	0.09	4.47E-02	4.45E-03	0.0126	5.62E-04	0.10	0.13	0.026
		lg_0.25_E_0.05_NC_yes_Da_2E-3	0.05	Yes	0.25	2E-03	3900	0.30	6.32E-10	7.19E+04	0.7	0.01	0.03	2.79E-02	2.78E-03	0.0506	5.62E-04	0.10	0.20	0.026
		lg_0.25_E_0.95_NC_yes_Da_2E-3	0.95	Yes	0.25	2E-03	3900	0.30	6.32E-10	7.19E+04	0.7	0.01	0.03	2.79E-02	2.78E-03	0.0506	5.62E-04	0.10	0.20	0.026
		lg_0.05_E_0.05_NC_no_Da_2E-3	0.05	No	0.05	2E-03	3900	0.54	6.32E-10	7.19E+04	0.7	0.01	0.11	5.03E-02	5.00E-03	0.0056	5.62E-04	0.10	0.11	0.026
		lg_0.05_E_0.95_NC_no_Da_2E-3	0.95	No	0.05	2E-03	3900	0.54	6.32E-10	7.19E+04	0.7	0.01	0.11	5.03E-02	5.00E-03	0.0056	5.62E-04	0.10	0.11	0.026
		lg_0.10_E_0.05_NC_no_Da_2E-3	0.05	No	0.10	2E-03	3900	0.48	6.32E-10	7.19E+04	0.7	0.01	0.09	4.47E-02	4.45E-03	0.0126	5.62E-04	0.10	0.13	0.026
		lg_0.10_E_0.95_NC_no_Da_2E-3	0.95	No	0.10	2E-03	3900	0.48	6.32E-10	7.19E+04	0.7	0.01	0.09	4.47E-02	4.45E-03	0.0126	5.62E-04	0.10	0.13	0.026
		lg_0.25_E_0.05_NC_no_Da_2E-3	0.05	No	0.25	2E-03	3900	0.30	6.32E-10	7.19E+04	0.7	0.01	0.03	2.79E-02	2.78E-03	0.0506	5.62E-04	0.10	0.20	0.026
		lg_0.25_E_0.95_NC_no_Da_2E-3	0.95	No	0.25	2E-03	3900	0.30	6.32E-10	7.19E+04	0.7	0.01	0.03	2.79E-02	2.78E-03	0.0506	5.62E-04	0.10	0.20	0.026
	St. II	lg_0.05_E_0.95_NC_yes_Da_2E-3*	0.95	Yes	0.05	2E-03	3900	0.54	6.32E-10	7.19E+04	0.7	0.01	0.11	5.03E-02	5.00E-03	0.0056	5.62E-04	0.10	0.11	0.026
		lg_0.25_E_0.95_NC_yes_Da_2E-3_D0	0.95	Yes	0.25	2E-03	3900	0.54	6.32E-10	7.19E+04	0.7	0.01	0.03	2.77E-02	5.11E-03	0.0306	5.62E-04	0.06	0.11	0.026
Permeability of the fabric (*Da*)		Da_4E-5_E_0.05_NC_yes_lg_0.2	0.05	Yes	0.20	4E-05	3900	0.36	1.26E-11	1.44E+03	0.7	0.01	0.05	3.35E-02	3.33E-03	0.0337	5.62E-04	0.10	0.17	0.026
		Da_4E-5_E_0.95_NC_yes_lg_0.2	0.95	Yes	0.20	4E-05	3900	0.36	1.26E-11	1.44E+03	0.7	0.01	0.05	3.35E-02	3.33E-03	0.0337	5.62E-04	0.10	0.17	0.026
		Da_2E-4_E_0.05_NC_yes_lg_0.2	0.05	Yes	0.20	2E-04	3900	0.36	6.32E-11	7.19E+03	0.7	0.01	0.05	3.35E-02	3.33E-03	0.0337	5.62E-04	0.10	0.17	0.026
		Da_2E-4_E_0.95_NC_yes_lg_0.2	0.95	Yes	0.20	2E-04	3900	0.36	6.32E-11	7.19E+03	0.7	0.01	0.05	3.35E-02	3.33E-03	0.0337	5.62E-04	0.10	0.17	0.026
		Da_2E-3_E_0.05_NC_yes_lg_0.2	0.05	Yes	0.20	2E-03	3900	0.36	6.32E-10	7.19E+04	0.7	0.01	0.05	3.35E-02	3.33E-03	0.0337	5.62E-04	0.10	0.17	0.026
		Da_2E-3_E_0.95_NC_yes_lg_0.2	0.95	Yes	0.20	2E-03	3900	0.36	6.32E-10	7.19E+04	0.7	0.01	0.05	3.35E-02	3.33E-03	0.0337	5.62E-04	0.10	0.17	0.026

Table B.1 (continued)

	Label	ε [-]	NC enabled	I_g [-]	*Da* [-]	*Re* [-]	U_{in} [m/s]	*K* [m^2]	Air permeability [L/min/m]	γ [-]	R_{ct}	k_s [W/K/m]	k_{fab} [W/K/m]	I_c [-]	H_{gap} [m]	H_{fab} [m]	D_0 [m]	D_1 [m]	k_f [W/K/m]
Permeability of the fabric (*Da*)	Da_4E-5_E_0.05_NC_no_Ig_0.2	0.05	No	0.20	4E-05	3900	0.36	1.26E-11	1.44E+03	0.7	0.01	0.05	3.35E-02	3.33E-03	0.0337	5.62E-04	0.10	0.17	0.026
	Da_4E-5_E_0.95_NC_no_Ig_0.2	0.95	No	0.20	4E-05	3900	0.36	1.26E-11	1.44E+03	0.7	0.01	0.05	3.35E-02	3.33E-03	0.0337	5.62E-04	0.10	0.17	0.026
	Da_2E-4_E_0.05_NC_no_Ig_0.2	0.05	No	0.20	2E-04	3900	0.36	6.32E-11	7.19E+03	0.7	0.01	0.05	3.35E-02	3.33E-03	0.0337	5.62E-04	0.10	0.17	0.026
	Da_2E-4_E_0.95_NC_no_Ig_0.2	0.95	No	0.20	2E-04	3900	0.36	6.32E-11	7.19E+03	0.7	0.01	0.05	3.35E-02	3.33E-03	0.0337	5.62E-04	0.10	0.17	0.026
	Da_2E-3_E_0.05_NC_no_Ig_0.2	0.05	No	0.20	2E-03	3900	0.36	6.32E-10	7.19E+04	0.7	0.01	0.05	3.35E-02	3.33E-03	0.0337	5.62E-04	0.10	0.17	0.026
	Da_2E-3_E_0.95_NC_no_Ig_0.2	0.95	No	0.20	2E-03	3900	0.36	6.32E-10	7.19E+04	0.7	0.01	0.05	3.35E-02	3.33E-03	0.0337	5.62E-04	0.10	0.17	0.026
Emissivity (ε)	E_0.05_Ig_0.25_NC_yes_Da_2E-3*	0.05	Yes	0.25	2E-03	3900	0.30	6.32E-10	7.19E+04	0.7	0.01	0.03	2.79E-02	2.78E-03	0.0506	5.62E-04	0.10	0.20	0.026
	E_0.35_Ig_0.25_NC_yes_Da_2E-3	0.35	Yes	0.25	2E-03	3900	0.30	6.32E-10	7.19E+04	0.7	0.01	0.03	2.79E-02	2.78E-03	0.0506	5.62E-04	0.10	0.20	0.026
	E_0.65_Ig_0.25_NC_yes_Da_2E-3	0.65	Yes	0.25	2E-03	3900	0.30	6.32E-10	7.19E+04	0.7	0.01	0.03	2.79E-02	2.78E-03	0.0506	5.62E-04	0.10	0.20	0.026
	E_0.95_Ig_0.25_NC_yes_Da_2E-3*	0.95	Yes	0.25	2E-03	3900	0.30	6.32E-10	7.19E+04	0.7	0.01	0.03	2.79E-02	2.78E-03	0.0506	5.62E-04	0.10	0.20	0.026

Appendix C Computational costs and mass/energy imbalances

Numerical simulation of the transport phenomena in the present setup (i.e. concentric geometry, limb surrounded by permeable fabric) with turbulent external flow ($Re = 3900$), and heat transfer by natural and forced convection, as well as radiation, can require an appreciable amount of time and computational resources. Table C.1 provides a summary of the computational costs associated with each simulation case, along with the obtained mass and energy imbalances. Mass imbalances were calculated according to equation G.1, and energy imbalances were calculated according to equations G.2 to G.5 (Appendix G). Energy imbalances were calculated in four different locations, in order to pinpoint the regions of the computational domain responsible for the most errors.

Table C.1: Computational costs and mass/energy imbalances, for each simulation case. Legend: NA - Not Available. *Reused cases from a different section.

Label			Computational costs			Mass imbalance [%]	Energy imbalance [%]			
			Simulation time [h]	Physical memory [GB]	Virtual memory [GB]	Global	Global	External (near microclimate)	Microclimate	Fabric
Air gap thickness ratio (l_g)	St. I	Ig_0.05_E_0.05_NC_yes_Da_2E-3	56	NA	NA	0.02	149	10	0.53	1.4
		Ig_0.05_E_0.95_NC_yes_Da_2E-3	57	NA	NA	0.02	149	8	0.35	0.8
		Ig_0.10_E_0.05_NC_yes_Da_2E-3	42	2.5	2.4	0.03	384	140	0.45	7.7
		Ig_0.10_E_0.95_NC_yes_Da_2E-3	42	2.6	2.6	0.03	271	77	0.15	3.2
		Ig_0.25_E_0.05_NC_yes_Da_2E-3	55	3.4	3.6	0.07	163	19	0.14	12.5
		Ig_0.25_E_0.95_NC_yes_Da_2E-3	56	3.4	3.6	0.06	138	11	0.10	3.8
		Ig_0.05_E_0.05_NC_no_Da_2E-3	77	2.4	2.6	0.01	144	9	0.48	0.8
		Ig_0.05_E_0.95_NC_no_Da_2E-3	66	2.4	2.6	0.01	144	7	0.33	0.6
		Ig_0.10_E_0.05_NC_no_Da_2E-3	47	2.7	2.5	0.03	289	151	0.36	3.4
		Ig_0.10_E_0.95_NC_no_Da_2E-3	45	2.8	2.6	0.03	265	76	0.08	1.0
		Ig_0.25_E_0.05_NC_no_Da_2E-3	48	3.5	3.7	0.06	175	32	0.10	26.8
		Ig_0.25_E_0.95_NC_no_Da_2E-3	57	3.5	3.7	0.06	125	9	0.05	4.4
	St. II	Ig_0.05_E_0.95_NC_yes_Da_2E-3*	57	NA	NA	0.02	149	8	0.35	0.8
		Ig_0.25_E_0.95_NC_yes_Da_2E-3_D0	56	2.6	2.7	0.10	333	85	0.28	9.4
Permeability of the fabric (Da)		Da_4E-5_E_0.05_NC_yes_Ig_0.2	43	3.0	3.2	0.01	143	17	0.07	6.8
		Da_4E-5_E_0.95_NC_yes_Ig_0.2	46	3.0	3.2	0.01	126	9	0.00	1.6
		Da_2E-4_E_0.05_NC_yes_Ig_0.2	38	2.8	2.9	0.01	145	17	0.05	6.5
		Da_2E-4_E_0.95_NC_yes_Ig_0.2	37	2.8	2.9	0.01	128	10	0.10	1.7
		Da_2E-3_E_0.05_NC_yes_Ig_0.2	45	2.9	3.1	0.06	161	19	0.25	11.4
		Da_2E-3_E_0.95_NC_yes_Ig_0.2	45	3.0	3.2	0.06	142	11	0.10	4.2
		Da_4E-5_E_0.05_NC_no_Ig_0.2	37	2.9	3.1	0.00	398	256	0.03	22.9
		Da_4E-5_E_0.95_NC_no_Ig_0.2	38	2.9	3.1	0.00	189	76	0.02	2.5
		Da_2E-4_E_0.05_NC_no_Ig_0.2	34	NA	NA	0.01	161	34	0.04	22.5
		Da_2E-4_E_0.95_NC_no_Ig_0.2	37	3.0	3.1	0.01	190	76	0.02	2.5
		Da_2E-3_E_0.05_NC_no_Ig_0.2	53	3.0	3.1	0.05	147	24	0.12	13.5
		Da_2E-3_E_0.95_NC_no_Ig_0.2	53	3.0	3.2	0.05	128	8	0.01	2.3
Emissivity of the inner fabric (ε)		E_0.05_Ig_0.25_NC_yes_Da_2E-3*	57	3.2	3.4	0.07	163	19	0.13	12.6
		E_0.35_Ig_0.25_NC_yes_Da_2E-3	56	3.2	3.4	0.07	146	13	0.11	6.7
		E_0.65_Ig_0.25_NC_yes_Da_2E-3	32	3.4	3.6	0.06	173	64	0.07	5.0
		E_0.95_Ig_0.25_NC_yes_Da_2E-3*	56	3.4	3.6	0.06	138	11	0.10	3.8

It should be noted that energy imbalances are relative values, in that they depend on the amount of energy that is lost at the skin. This approach (i.e. the division by average energy loss at the skin) was chosen because it provides the tightest criterion for the evaluation of the quality of settings and subsequent results. That being the case, the very large values that are obtained for the global energy imbalances (over $100\ \%$) mean only that the energy that is lost (or gained) in the entire system is higher than the energy loss at the skin, which is actually quite low in some cases. These high values, however, do cause some concerns regarding the obtained results in the microclimate and at the fabric, and that is why imbalances were calculated in three other regions: external (near microclimate) – between the skin and an imaginary external boundary at some distance from the clothing layer; microclimate – between the skin and the inner fabric; fabric – between the inner fabric and the outer fabric. External energy imbalances were, in almost all cases, less than half of the global imbalances, meaning that the gross of the errors is located in the regions farthest from the clothed limb. Imbalances in the microclimate were lower than $1\ \%$, whereas imbalances at the fabric varied between less than $1\ \%$ to over $26\ \%$. It was noticed that the largest percentage errors at the fabric were obtained for the cases where the emissivity of the inner fabric was $\varepsilon = 0.05$, which is most likely due to the fact that the energy exchange at the skin (the denominator in the energy imbalance equations) is lower (Section 4.3). For the same reason, imbalances also increase with decreasing fabric permeability.

It was suspected that imbalances at the fabric may partially be caused by an incomplete coupling of the energy-related variables between the two COMSOL interfaces “Free and Porous Media Flow” and “Turbulent Flow”, namely the turbulent kinetic energy. Results for this latter variable around the fabric, however, show that its value is very low, so its contribution should not majorly affect the total energy in the microclimate.

In sum, energy imbalance results, in addition to the validation study (Appendix D), seem to indicate that the mesh used was refined enough in the regions close to the microclimate to produce grid-independent results. This is because the majority of errors come from the far edges of the computational domain, where the mesh was coarsest, and are not likely to significantly affect the results calculated within the clothed limb. This study could, nonetheless, benefit from additional grid independence testing, specifically for the cases where the imbalances were highest ($\varepsilon = 0.05$).

Appendix D Validation of the numerical methods and grid independence analysis

Validation of the numerical models for the geometry and conditions relevant to this study were performed by comparing the obtained results with those of the reference authors, following different numerical approaches (Sobera et al. 2003; Sobera 2006; Sobera & Kleijn 2008). This was achieved by using the same values for all dimensionless parameters ($Re = 3900$; $I_\mathrm{g} = 5 \times 10^{-2}$; $I_\mathrm{c} = 5 \times 10^{-3}$; $Da = 2 \times 10^{-3}$) and boundary conditions as the latter authors. Heat transfer by radiation and by natural convection was not considered in this study, as these phenomena were not considered by the reference author. The turbulence model used (LRN $k - \varepsilon$) differed from that of the reference study (RNG), because the latter was not available in COMSOL Multiphysics.

Testing for grid independence was accomplished by comparing results related to flow and heat transfer for three increasingly refined meshes (please refer to Appendix A for a representation of the meshes), with an increasing number of elements. The mesh used in parametric studies was then chosen in a compromise between accuracy of the obtained results and the computational costs involved.

Figure D.1 and D.2 show some flow and heat transfer related results, respectively, obtained using the three different meshes, along with reference results. Table D.1, in turn, shows a summary of the computational costs, mass and energy imbalances, average Nusselt number and Strouhal number, obtained using each of the three meshes.

Table D.1: Results obtained for computational costs, mass and energy imbalances, and average Nusselt and Strouhal numbers. Numbers between brackets show the percentage difference between results obtained for the respective mesh and those obtained for the preceding coarser mesh. Please refer to Appendix G for formulae. Legend: NA-Not Applicable.

		Mesh 1		**Mesh 2**		**Mesh 3**	
Number of grid elements		38'038		87'836		230'664	
Solution time [h]		18		39		110	
Physical memory [GB]		2.3		2.9		5.8	
Virtual memory [GB]		2.3		3.1		6.1	
Mass imbalance [%]		0.004		0.080		0.173	
Energy imbalance [%]	**Global**	206		236		344	
	Microclimate	0.57		0.39		0.16	
	Fabric	3.30		3.12		3.06	
	External (near microclimate)	14		23		70	
Nu_{avg}		14.52	(NA)	14.40	(0.84)	14.36	(0.26)
St **[-]**		0.225	(NA)	0.229	(1.86)	0.230	(0.52)

There was found to be a good qualitative agreement between present results and those obtained by reference authors. There were, however, some quantitative differences: the recirculation length (i.e. the x-wise distance in which the velocity u is negative), for example, is over-predicted in the present results (for Mesh 1) by $40\ \%$ (Figure D.1a). Present tangential velocity ratio results seem to be underestimated by up to $65\ \%$, particularly in the downstream regions, when compared to Direct Numerical Simulation (DNS) results (Figure D.1b, grey lines compared to full black line). Tangential velocity results almost match those obtained by reference authors for 2D simulations, possibly indicating that the effect of the third dimension is not negligible (Figure D.1b, grey lines compared to dash-dotted black line). Deviations in Nusselt number around the skin reach about $50\ \%$ (Figure D.2, grey lines compared to full black line).

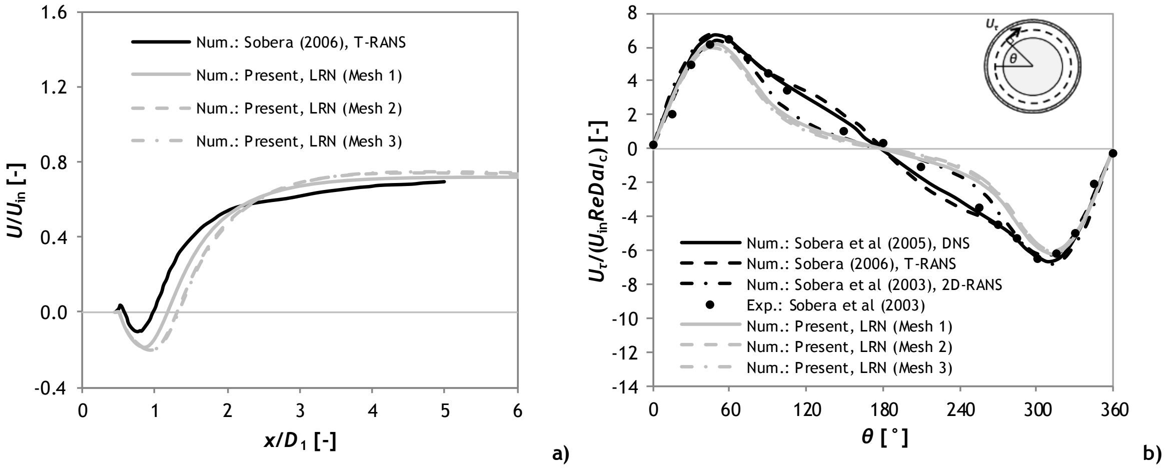

Figure D.1: Time-averaged streamwise velocity ratio along the centerline (a) and tangential velocity ratio around the microclimate (b), obtained using three different meshes. Legend: Num.- Numerical; Exp.- Experimental.

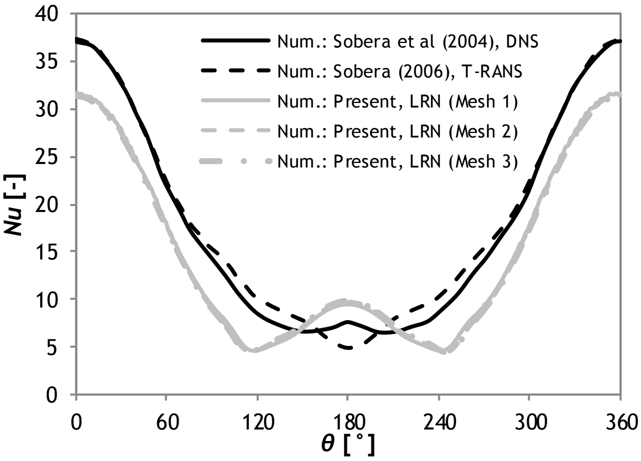

Figure D.2: Time-averaged Nusselt number around the skin (boundary 3, Figure 3.1b).

Comparison with reference results shows that there are quantitative disagreements with results obtained presently. It is hypothesised that this may be due to an inadequacy of the LRN $k - \varepsilon$ turbulence model, or to having neglected the third dimension. Nevertheless, these discrepancies did not undermine the more complete (parametric) study performed in this thesis, as the curves show a similar qualitative behaviour.

Mesh 1 was chosen for the parametric studies, even though results for streamwise velocity ratio were not yet fully mesh independent. This was because results for tangential velocity ratio around the microclimate and for Nusselt around the skin practically did not vary when the mesh was refined (Figure D.1b and D.2, grey lines). Table D.1 shows that time- and space-averaged Nusselt number and Strouhal number did not significantly vary with increasing the number of elements in the mesh. The choice of Mesh 1, instead of Mesh 2, also allowed to reduce computation time by half, and to save on file size, thereby minimizing the computational costs.

Table D.1 also displays the obtained energy imbalances for each mesh. The high values observed for the global imbalances are discussed in some detail in Appendix C, and the formulas used are available in Appendix G. Ideally, Mesh 3 should have been further refined until energy imbalances were under $\sim 10\ \%$. This was not feasible, because the time and memory requirements to accomplish it would be too high. Computational costs were indeed the bottleneck for this project, as it would not be possible to conduct such a comprehensive study using a denser mesh.

Appendix E Turbulence model comparison

The Reynolds number used throughout this thesis (3900) meant that flow outside the clothed limb was turbulent. This required the use of a turbulence model in order to adequately simulate flow in the external domain. Sobera (2006) obtained good results when using the Re-Normalization Group (RNG) $k - \varepsilon$ model, but unfortunately, this model has not yet been made available in COMSOL Multiphysics. Two of the turbulence models offered in this software were considered to be good candidates for this purpose: the Low Reynolds Number (LRN) and the Shear Stress Transport (SST). In this section, flow results obtained using the two different turbulence models for the case of a bare cylinder (unclothed limb) at $Re = 3900$ are presented and compared to published results numerical and experimental results (Sobera et al. 2004; Sobera 2006; Norberg 1987; Tremblay 2001; Breuer 1998).

Figure E.1 shows that the LRN turbulence model is in slightly better agreement with reference DNS results. The better suitability of the LRN model is further observed in Table E.1, where LRN results present much lower deviations from average experimental results from Norberg (1987) and Tremblay (2001). Because of this, the LRN turbulence model was considered more appropriate, even though discrepancies between DNS results were still appreciable.

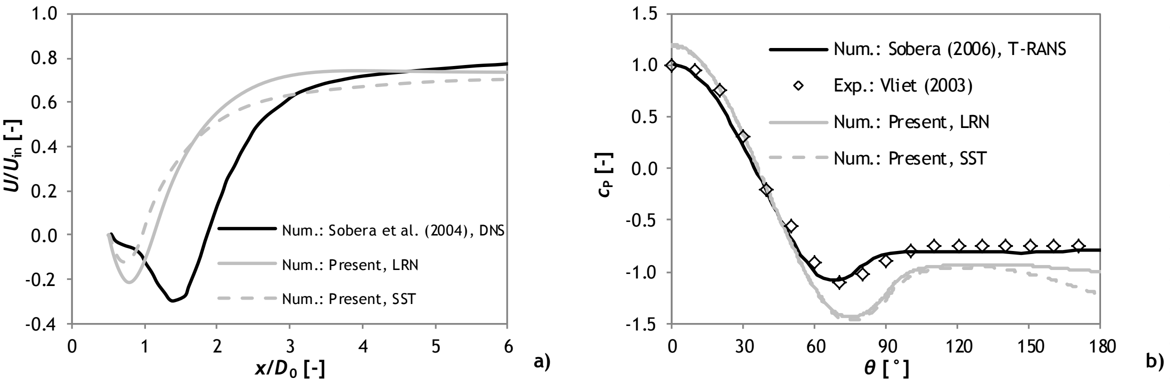

Figure E.1: Time-averaged normalized streamwise velocity ratio along centerline (a) and pressure coefficient around the bare limb, obtained using LRN and SST turbulence models, compared to numerical and experimental results by reference authors. Legend: Num.-Numerical; Exp.- Experimental.

Table E.1: Result comparison between different approaches for simulation of fluid flow around bare cylinder at $Re = 3900$ and published numerical and experimental results. Numbers between brackets show the relative difference between each physical property and the averaged results between the experimental studies by Norberg (1987) and Tremblay (2001). Legend: Num.-Numerical; Exp.- Experimental; NA-Not Applicable/Not Available.

Author	Type of study	St [-]	c_D [-]	$c_{P,b}$ [-]	L_{rec}/D_0 [-]
Norberg (1987)	Exp.	0.212 (NA)	0.98 (NA)	-0.84 (NA)	NA (NA)
Tremblay (2001)	Exp.	0.215 (NA)	0.99 (NA)	-0.88 (NA)	1.4 (NA)
	Num.: DNS	0.220 (3.04)	1.03 (4.57)	-0.93 (8.14)	1.3 (7.14)
Breuer (1998)	Num.: LES	0.215 (0.70)	1.016 (3.15)	-0.941 (9.42)	1.372 (2.00)
Sobera (2006)	Num.: T-RANS	0.205 (3.98)	NA (NA)	-0.789 (8.26)	1.31 (6.43)
Present study	Num.: Laminar	0.251 (17.44)	1.497 (51.96)	-1.236 (43.76)	0.001 (99.91)
	Num.: SST	0.238 (11.67)	1.263 (28.19)	-1.205 (40.07)	0.469 (66.51)
	Num.: LRN	0.226 (5.80)	1.096 (11.23)	-0.995 (15.68)	0.626 (55.31)

Appendix F Influence of the reference temperature on the heat flux results at the fabric

Time-averaged local heat fluxes around the fabric were observed to widely vary with the chosen reference temperature. That is because the convective component of the heat fluxes ($cflux$) is calculated according to equation F.1, so it is a function of the specific enthalpy of the air that enters/leaves the microclimate.

$$cflux = \rho\vec{U}H - \vec{U}p \tag{F.1}$$

Enthalpy is not an absolute quantity, but instead a relative quantity that depends on the reference state (i.e. the reference enthalpy and temperature). Figure F.1 illustrates the dependence of the total and convective heat fluxes around the fabric with the reference temperature.

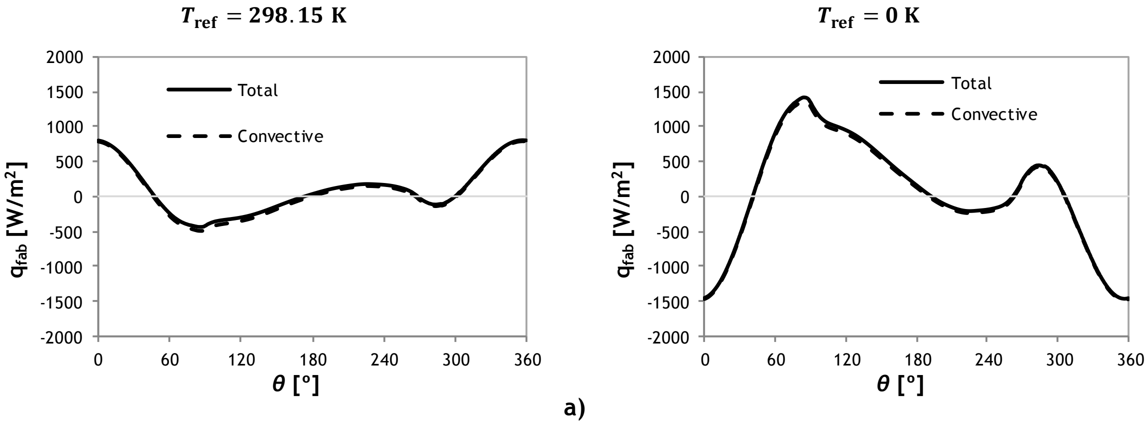

a) b)

Figure F.1: Time-averaged total and convective heat fluxes around the fabric (boundary 5, Figure 3.1b), obtained using two different reference temperatures: a) $T_{ref} = 298.15$ K; b) $T_{ref} = 0$ K. Negative fluxes mean that heat is entering the microclimate, while positive fluxes signify that heat is exiting it.

While both representations of the heat fluxes at the fabric are correct at their respective reference temperature, the one where $T_{ref} = 0\,\mathrm{K}$ provides a more straightforward interpretation of the results. As an example, let us compare results at the two different reference temperatures, at $0 < \theta < 41°$ (Figure F.1a compared to F.1b): when $T_{ref} = 298.15\,\mathrm{K}$, heat fluxes are positive, which can mean that heat is either exiting the microclimate, or that it is entering the microclimate at a temperature below T_{ref}; when $T_{ref} = 0\,\mathrm{K}$, heat fluxes are negative, meaning that heat enters the microclimate at a temperature above T_{ref} $(0\,\mathrm{K})$. Because of this, $T_{ref} = 0\,\mathrm{K}$ was deemed more suitable for the analysis of results in this study.

Appendix G Formulae

Formulae used throughout this study for the obtainment of relevant physical quantities, as well as mass and energy imbalances are hereby presented.

Mass imbalances were calculated in order to ensure convergence, by applying the integral of the x-velocity over the inlet and outlet boundaries:

$$Mass\ imbalance\ [\%] = \frac{\int u\ dl|_{\mathrm{out}} - \int u\ dl|_{\mathrm{in}}}{\int u\ dl|_{\mathrm{in}}} \times 100 \tag{G.1}$$

where l is the arc length. Energy imbalances were calculated according to equations (G.2) to (G.5).

$$Global\ energy\ imbalance\ [\%] = (\int E_{\mathrm{total}}\ dl|_{\mathrm{skin}} + \int E_{\mathrm{total}}\ dl|_{\mathrm{in}} - \int E_{\mathrm{total}}\ dl|_{\mathrm{out}} - \int \frac{dE}{dt}\ dA\Big|_{\mathrm{microclimate}} - \int \frac{dE}{dt}\ dA\Big|_{\mathrm{fabric}} - \int \frac{dE}{dt}\ dA\Big|_{\mathrm{external\ domain}}) / \int E_{\mathrm{total}}\ dl|_{\mathrm{skin}} \times 100 \tag{G.2}$$

$$Energy\ imbalance\ between\ skin\ and\ external\ boundary\ (near\ microclimate)\ [\%] = (\int E_{\mathrm{total}}\ dl|_{\mathrm{skin}} + \int E_{\mathrm{total}}\ dl|_{\mathrm{external\ boundary}} - \int E_{\mathrm{total}}\ dl|_{\mathrm{out}} - \int \frac{dE}{dt}\ dA\Big|_{\mathrm{domain}}) / \int E_{\mathrm{total}}\ dl|_{\mathrm{skin}} \times 100 \tag{G.3}$$

$$Energy\ imbalance\ in\ the\ Microclimate\ [\%] = (\int E_{\mathrm{total}}\ dl|_{\mathrm{skin}} - \int E_{\mathrm{total}}\ dl|_{\mathrm{inner\ fab}} - \int \frac{dE}{dt}\ dA\Big|_{\mathrm{microclimate}}) / \int E_{\mathrm{total}}\ dl|_{\mathrm{skin}} \times 100 \tag{G.4}$$

$$Energy\ imbalance\ in\ the\ Fabric\ [\%] = (\int q_{\mathrm{total}}\ dl|_{\mathrm{inner\ fab}} - \int q_{\mathrm{total}}\ dl|_{\mathrm{outer\ fab}} - \int \frac{dE}{dt}\ dA\Big|_{\mathrm{fab}}) / \int E_{\mathrm{total}}\ dl|_{\mathrm{skin}} \times 100 \tag{G.5}$$

Recirculation length was defined in this study as the x-wise distance in which the velocity u is negative, and can be written as follows, where x_{rec} is the x coordinate at the end of the negative velocity region, and x_{e} the coordinate at the cylinder's back stagnation point.

$$L_{\mathrm{rec}} = x_{\mathrm{rec}} - x_{\mathrm{e}} \tag{G.6}$$

Thermal resistance of the fabric, R_{CT}, was kept constant in every simulation, and is expressed by equation G.7, where A_{skin} is the surface area of the skin (boundary 3), and A is the logarithmic average between the areas of the inner and outer surfaces of the fabric (boundaries 4 and 5).

$$R_{\mathrm{CT}} = A_{\mathrm{skin}} \frac{H_{\mathrm{fab}}}{k_{\mathrm{fab}} A} = \frac{D_0 \ln(1 + \frac{H_{\mathrm{fab}}}{D_0/2 + H_1})}{2\, k_{\mathrm{fab}}} \tag{G.7}$$

As far as the tangential velocity component, it was calculated using equation G.8:

$$\frac{U_\tau}{U_{\mathrm{in}}\, Re\, Da\, Ic} = \frac{u \cos\left(\frac{\pi}{2} - \theta\right) + v \sin(\frac{\pi}{2} - \theta)}{U_{\mathrm{in}}\, Re\, Da\, Ic} \tag{G.8}$$

Four dimensionless numbers were also calculated using the expressions shown in G.9 to G.12. The oscillating behaviour of the flow is evaluated by the Strouhal number, St:

$$St = \frac{f\, D_1}{U_{\mathrm{in}}} \tag{G.9}$$

where f is the frequency of vortex shedding and D_1 the diameter of the outer surface of the fabric.

The time-averaged total Nusselt number is given by:

$$Nu = \frac{\frac{1}{t_{\max} - t_0} \int_{t=t_0}^{t=t_{\max}} q_{\mathrm{total}}(t) \times D_1\, dt}{k_{\mathrm{f}}(T_{\mathrm{skin}} - T_{\mathrm{air}})} \tag{G.10}$$

with t_0 being the first time at which flow can be considered periodic, $t_{\max}$ the final flow time, and k_{f} the thermal conductivity of the fluid.

For the cases where free convection is enabled, it becomes relevant to analyse the Grashof number, which gives the ratio of buoyant to viscous forces:

$$Gr = \frac{\beta\, g\, \left(T_{\mathrm{skin}} - T_{\mathrm{avg\ inner\ fab}}\right) {H_{\mathrm{gap}}}^{3}\, \rho^{2}}{\mu^{2}} \tag{G.11}$$

with β being the thermal expansion coefficient, g the acceleration of gravity, H_{gap} the thickness of the gap between the skin and the fabric, ρ the density of the fluid, μ its viscosity, and $T_{\mathrm{avg\ inner\ fab}}$[3] the average temperature of the inner fabric boundary.

Finally, in order to evaluate the onset of natural convection it can also be useful to look at the Rayleigh number, defined as follows:

$$Ra = Gr \times \frac{C_{\mathrm{p}}\, \mu}{k_{\mathrm{f}}} \tag{G.12}$$

The time-dependent results from all the above dimensionless numbers obtained in COMSOL were afterwards time-averaged using a post-processing script in MATLAB Livelink.

---

[3] The average temperature around the inner fabric was obtained by calculating the integral of the temperature over the inner fabric ($\mathrm{K\,m^2}$), and dividing it by the area of the surface of integration.